LOEFFLER, SHANE E. Ph.D. *In silico* electrocardiogram from simplistic geometric and reaction diffusion model for detection of cardiac ventricular abnormalities through machine learning methods (2021)
Directed by Dr. Joseph Starobin. 92 pp.

Millions of people around the globe die each year from ischemic heart disease. While previous work has focused on the detection of myocardial scarring after an ischemic event, there is little to no work that involves the detection of ventricular ischemia in the early stages of an ischemic event. Using simplified geometries and standard electrophysiological modeling, normal and ischemic conditions may be simulated within a left ventricle model. This work highlights the theoretical framework for determining the configuration of myocardial ischemia using analytical and deep learning methods. Using these methods, a two-dimensional model was used to find a theoretical threshold that can dictate when normal transmural myocardial ischemia is occurring. Using a three-dimensional model, 20,000 stochastic ischemic zones were simulated with associated ECGs to train a one-dimensional convolutional neural network to predict the configuration of the early stages of ischemia. In addition, a three-dimensional model was implemented to produce 10,000 stochastically growing ischemic configurations in which a one-dimensional convolutional and long-short term memory neural network was used to predict the future states of ischemia.

IN SILICO ELECTROCARDIOGRAM FROM SIMPLISTIC GEOMETRIC AND REACTION DIFFUSION MODEL FOR DETECTION OF CARDIAC VENTRICULAR ABNORMALITIES THROUGH MACHINE LEARNING METHODS

by

Shane E. Loeffler

A Dissertation

Submitted to

the Faculty of The Graduate School at

The University of North Carolina at Greensboro

in Partial Fulfillment

of the Requirements for the Degree

Doctor of Philosophy

Greensboro

2021

Approved by

Dr. Joseph Starobin
Committee Chair

DEDICATION

This work is dedicated to my wife, children, and family who I cherish dearly.

APPROVAL PAGE

This dissertation written by Shane E. Loeffler has been approved by the following committee of the Faculty of The Graduate School at The University of North Carolina at Greensboro.

Committee Chair

Dr. Joseph Starobin

Committee Members

Dr. Hemali Rathnayake

Dr. Tetyana Ignatova

Dr. Kristen Rhinehardt

November 1, 2021

Date of Acceptance by Committee

October 11, 2021

Date of Final Oral Examination

ACKNOWLEDGEMENTS

The work shown in this dissertation comes from years of effort that would truly not be possible with the people nearest to me. While there were some bumps along the way, without the people who cared for me, I do not know where I would be today; probably not here.

I would like to thank Dr. Starobin, who has guided me throughout my PhD program. He has taught me so much about life and research that I do not know how else to thank him than to have it written here. I thank my committee members: Dr. Hemali Rathnayake, Dr. Tetyana Ignatova, and Dr. Kristen Rhinehardt, for taking the time to help me along the way and for examining my work. I would like to thank all the other professors at JSNN and Dean Obare, each for being mentors to me in one way or another. I would like to thank my previous professors Dr. Ian Beatty and Dr. William Gerace, who helped me learn to enjoy physics. I would also like to thank my lab mates for listening to me and taking time out of their own busy lives to help me along the way. I also want to say thank you to my classmates, who helped me in both my personal and professional life.

Finally, I want to thank my wife, Adilene Lopez, for supporting me throughout my entire PhD; my son Abraham who gives me smiles every day; my future children who I know will brighten my heart; my parents and siblings, who listened to me talk about my work even if they had no clue what I was talking about; my friends old and new who have walked with me through life; and finally, most importantly, God, who has helped me through all my struggles, calmed my heart, loved me, and has given me hope in my life.

TABLE OF CONTENTS

LIST OF TABLES

LIST OF FIGURES

CHAPTER I: INTRODUCTION

Heart disease is responsible for millions of deaths worldwide in 2019. Within the United States there were over 800,000 heart disease deaths in 2018[1].While regular medical visits can preemptively help diagnose or prevent heart disease there are still many cases which go undetected and cause major complications or death. Of all the heart diseases the worse is coronary heart disease (CHD), which is the narrowing of the coronary arteries and leads to ischemic heart disease (IHD). CHD/IHD accounts for 42.1% of heart disease deaths every year[1]. Previous studies have shown the ability to determine IHD using a 12-lead electrocardiogram (ECG)[2]. While other methods exist to determine ischemia, the ECG is preferred because it is non-invasive, inexpensive, and standard in most clinical settings. While the standard 12-lead ECG works well, if a smaller portable device could provide similar results as an ECG, then IHD deaths could be lowered. Unfortunately, not much work has been done to preemptively determine and track ischemia using a small device.

For this work we will focus on theoretically determining and predicating IHD using non-invasive measurements in conjunction with Artificial Intelligence (AI) and traditional methods. This work focuses on using reaction diffusion differential equations to represent the cellular and bulk dynamics of the myocardium to produce *in silico* ECGs. *In silico* ECGs are processed using AI and traditional methods for determining and predicting IHD. Simple geometries, which approximate the left ventricle, are used to produce ECGs. Using simple geometries allows for large amount of data to be produced while still providing accurate results. Typically, AI requires large amounts of data to train the model for predictions.

AI will be defined as any method which allows a computer program to update itself to mimic human predictions. AI encompasses different methods such as decision trees, random

forests, linear and non-linear regression, k-nearest neighbors, neural networks, etc. Training of an AI model can be either supervised or unsupervised. Supervised learning focuses on connecting data based on inputs and outputs whereas unsupervised learning finds patterns of input data only. Roughly speaking, supervised learning is used to solve problems of the form $Y = f(X)$ where the function is the supervised model. This work focuses on supervised deep learning with neural networks.

Knowledge Gap

The heart acts as a bioelectrical pump to move blood throughout the body. In humans the heart is composed of four chambers which expand and contract when electrically stimulated to pump blood Figure 1.

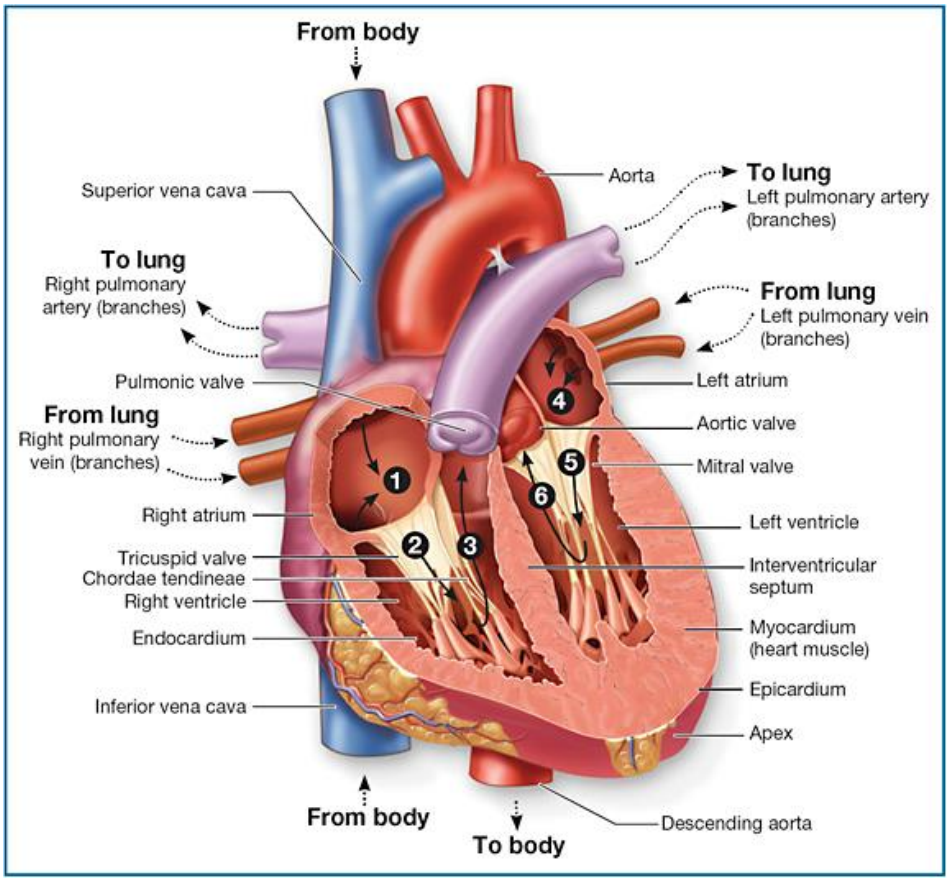

Figure 1 – Anatomy of the human heart. Reproduced from Ellis[3].

The four chambers are the left and right atriums (LA and RA, respectively) and the left and right ventricles (LV and RV, respectively). The LV has the greatest mass of all four chambers being 217% larger than the right ventricle which is the second largest chamber[4]. Having the greatest mass allows the LV to produce most of the electrical activity within the heart. Excitation of the ventricles is caused by neural muscular junctions which couple the myocardium to the Purkinje fibers (PF). PF are a fibrous network of nerves found within the sub-endocardium region of the ventricle. PF have ionic waves which propagate at $2-3\ \frac{m}{s}$ which is about 10 times greater the speed of the ionic waves which propagate through the myocardium[5].

Ischemia is a cardiac disease in which the coronary arteries, which provide oxygenated blood to the heart, become occluded which disrupts the cellular function of the myocardium and can lead to injury or death. When ischemia occurs, it typically starts from a small region and grows outwards at an unpredictable rate. Ischemia can occur over a long period of time or can occur abruptly. When myocardial cells stop receiving oxygenated blood, they become less excitable until they become non-excitable, necrotic and fibrosis. Ischemia typically occurs in the LV and rarely occurs elsewhere. Ischemia in the RV rarely occurs without being in the LV as well [6–8]. Typically, ischemia is diagnosed through lab tests or electrocardiogram (ECG).

The ECG is a machine which determines the electrical activity of the heart based upon the body surface potential. Typical ECG use 12 leads which consist of 10 electrodes to determine the current that the heart produces in 12 different axes. Axes are determined based upon the location of the electrodes with respect to one another and the heart.

Previous research has focused on using high resolution meshes to simulate the bio-electrical activity of the heart. These meshes typically use finite element method (FEM) to compute *in silico* ECGs. FEM works well in complex geometries but requires more

computational power compared to finite difference method (FDM). This work makes use of simplified geometries that accurately reflect the shape of the left ventricle to compute *in silico* ECGs in a timely matter using FDM.

Other research has been able to determine ischemic tissue in discrete locations using AI with real ECGs with high accuracy. The ECG data was previous annotated by clinicians with the location of ischemia in discrete placements. Typically, the AI will use classification methods to only determine where and if ischemia has occurred within the ventricles. No previous work has included ischemic zones that have different degrees of severity of ischemia in which the cells are in a state of less excitability. The work presented in this paper strives to apply AI methods to determine a continuous output of the location and severity of ischemia via regression. In addition, exploration into predicting future states of ischemia using AI or other methods are detailed in this work which may be able to track and preemptively predict an ischemic event.

Background

Numerical Approximations

Many biophysical systems can be described using differential equations but normally feature non-linear functions. Typically, these non-linear systems, if they cannot be transformed, are not solvable by analytical method. Solutions to non-linear differential equations are usually solved using numerical approximations. Numerical approximations are mathematical schemes which use finite differences to solve differential equations in place of infinitesimal differences. Finite difference method (FDM) approximates a differential using a truncated version of a Taylor series expansion. A Taylor series expansion is described in (1). The difference between (1) using the + and − respectively is described by (2) and in the same manner the addition of the same two equations is described by (3).

$$f(x \pm h) = f(x) \pm h\, f'(x) + h^2 \frac{f''(x)}{2!} \pm \cdots = \sum_{n=0}^{\infty} h^n \frac{f^{(n)}(x)}{n!} \quad \textbf{(1)}$$

$$f(x + h) - f(x - h) = 2\, h\, f'(x) + \mathcal{O}(h^3) \quad \textbf{(2)}$$

$$f(x + h) + f(x - h) = 2\, f(x) + 2\, h^2 \frac{f''(x)}{2!} + \mathcal{O}(h^4) \quad \textbf{(3)}$$

Removing the truncation error, $\mathcal{O}$, approximates (2) and (3) to an order of accuracy h^2. (2) and (3) can be used in place of a differential to numerically solve differential equations using discretized grids of a system both spatially and temporally.

Cellular Dynamics

Within the heart, there are specific cells that have proteins embedded in their membranes which control the concentration of ions in the extracellular and intracellular matrix. These proteins consist of ion channels, transporters and pumps and are collectively referred to as gates. Channels and transporters are usually passive and allow ions to move in the direction of the concentration gradient. Pump proteins are active and usually move ions across the cellular membrane in directions against the concentration gradient.

Cells which contain gates are usually considered excitable and can typically perform mechanical functions or propagate bioelectrical signals depending on the state of the cell. The difference of ion concentrations inside and outside the cell cause a potential gradient across the membrane of the cell called the transmembrane potential (V_m or u) which is defined as $u = V_{Out} - V_{in}$ where V_{in} and V_{out} are the potentials inside and outside the cell, respectively. When excited, these cells exhibit a changing transmembrane potential due to the controlled flow of ions

inside and outside the cell which is called an action potential (AP). The dynamics of the gates have been shown to open and close based upon the transmembrane potential and the current state of the gate. The dynamics of the gates may be described using non-linear differential equations. These equations describe the permeability of the gates that are either closed or open defined as 0 and 1, respectively. Typically, the kinetics of the gates are controlled by two function which describe the activation and inactivation dynamics of the gate. The permeability of the gates is described in the general form (4).

$$\frac{dn}{dt} = \alpha[u] * (1 - n) - \beta[u] * n \quad \textbf{(4)}$$

u is the transmembrane potential and n is the variable describing the permeability of the gate. The activation functions α and β are fitted from experimental data and are modeled by (5) and (6)

$$\alpha[u] = \frac{\alpha_\infty[u]}{\tau_\alpha[u]} \quad \textbf{(5)}$$

$$\beta[u] = \frac{1 - \beta_\infty[u]}{\tau_\beta[u]} \quad \textbf{(6)}$$

α_∞ and β_∞ are the steady state of activation and inactivation, respectively. The steady state functions are fitted from experimental data as well. Both the activation and inactivation function have a period function, τ_α and τ_β, that are fitted experimentally, and define how quickly the gates open and close depending on the transmembrane potential.

The total current across the cellular membrane is related to the transmembrane potential. Protein gates control the permeability of ionic currents across the cellular membrane. When all gates of a certain type are open then the conductivity approaches the maximum value found experimentally. The general relationship for an ionic current is described by (7).

$$J = g_{max} * f[\vec{n}] * (u - u_O) \tag{7}$$

Where g_{max} is the maximum conductance for the current, $f[\vec{n}]$ is a permeability function in which a single or multiple gate variable are inputs and output is a scaler between 0 and 1, u is the transmembrane potential and u_o is the Nernst potential for the specific ion type. During an AP, when there is no net movement across a membrane of a particular ion the transmembrane potential is equal to the Nernst Potential. A summation of all the Nernst potentials, for all ions that cross the cellular membrane of a cell, is the resting potential.

The total current across a cellular membrane is found using the superposition principle in which the total current across the membrane is the sum of all the individual ionic currents across the membrane. This is described by (8).

$$C_m \frac{du}{dt} = -\sum_i J_i = \sum_i g_{max,i} * f_i[\vec{n}] * \left(u - u_{O_i}\right) \tag{8}$$

Where C_m is the capacitance of the membrane and the summation is over all the ionic currents across the cellular membrane including a stimulus current. A stimulus current is an external current that raises the transmembrane potential enough to begin an AP cycle. In the

ventricles of the heart, the stimulus current comes from the neuromuscular junctions between the Purkinje fibers and the myocardium. Neuromuscular junctions release ions which stimulate the surrounding myocardial cells to begin an AP.

Multicellular Dynamics

When cells are connected to each other through gap junction, the ionic currents from one cell affect the surrounding cells. This changes the transmembrane potential of the surrounding cell and the surrounding cells become excited and begin their own AP. This process continues from cell to cell and creates a reaction-diffusion wave. A reaction-diffusion wave is described by adding a diffusive current to (8) and describes the propagation of ionic concentrations from one cell to another. This process is described by (9).

$$C_m \frac{du}{dt} + \sum_i J_i = \nabla \cdot \left(\widetilde{D} \nabla u\right) \tag{9}$$

Where $\widetilde{D}$ is the diffusion tensor, ∇ is the gradient operator and $\nabla \cdot$ is the divergence operator. The inclusion of the diffusive current describes the propagation of AP from cell to cell. In many situations, $\widetilde{D}$ is equal in all directions and the diffusive current is defined as homogeneous in the form $\widetilde{D}\nabla^2 u$. When diffusion is not equal in all directions the diffusive current may be expanded as described by (10).

$$\nabla \cdot \left(\widetilde{D} \nabla u\right) = \nabla u \cdot \left(\nabla \cdot \widetilde{D}\right) + \widetilde{D} : \nabla(\nabla u) \tag{10}$$

Where the operator : is a double dot or double contraction.

Fitzhugh-Nagumo

One of the simplest systems of equations that can represent the electrophysiological dynamics of a cell is the Fitzhugh-Nagumo model (FN) [9–11]. FN was originally developed to simplify the dynamics of nerve cells originally proposed by Hodgkin and Huxley in 1952[12]. FN reflects the general dynamics of cardiomyocyte cells and uses two functions to represent all the ionic currents across the cellular membrane. This includes a non-linear transmembrane dependent current to describe the behavior of the cellular membranes' excitation and a recovery current that returns an excited cell to a resting potential state. For a single cell, FN is described by (11) and (12).

$$C_m \frac{\partial u}{\partial t} = -A\,(u - u_{rest})(u - u_{threshold})(u - u_{max}) - v + J_{Stim} \quad \textbf{(11)}$$

$$\frac{\partial v}{\partial t} = \varepsilon(\beta u - v) \quad \textbf{(12)}$$

Where C_m is the capacitance of the cellular membrane, u is the transmembrane potential and v is the recovery current, A is the variable which scales the cubic current, u_{rest} is the resting potential value, $u_{threshold}$ is the potential that needs to be crossed to activate the quick Na channels to start an AP cycle, J_{Stim} is the external current to excite the cell, β is the period that u takes to change the recovery current and ε is the ratio between how quickly the ionic channels open to how slowly the ionic channels close and typically $\varepsilon \ll 1$.

To analyze the FN model, the nullclines and vector plot describe how the system will behave depending on the state of the system. Nullclines describe a differential system's behavior when the change of all functions are zero. The vector plot describes the change in the systems'

variables based upon the current state of the system. For FN model, the nullclines are found by solving (11) and (12) such that both $\frac{\partial u}{\partial t}$ and $\frac{\partial v}{\partial t}$ are equal to zero. Assuming that J_{Stim} is zero for most of the AP, FN nullclines are defined by (13) and (14).

$$\frac{\partial u}{\partial t} = 0 \;\rightarrow\; v = -A\,(u - u_{rest})(u - u_{Threshold})(u - u_{max}) \tag{13}$$

$$\frac{\partial v}{\partial t} = 0 \;\rightarrow\; v = \beta u \tag{14}$$

The phase space between the variables u and v contain both the nullclines and vector fields and is shown in Figure 2.

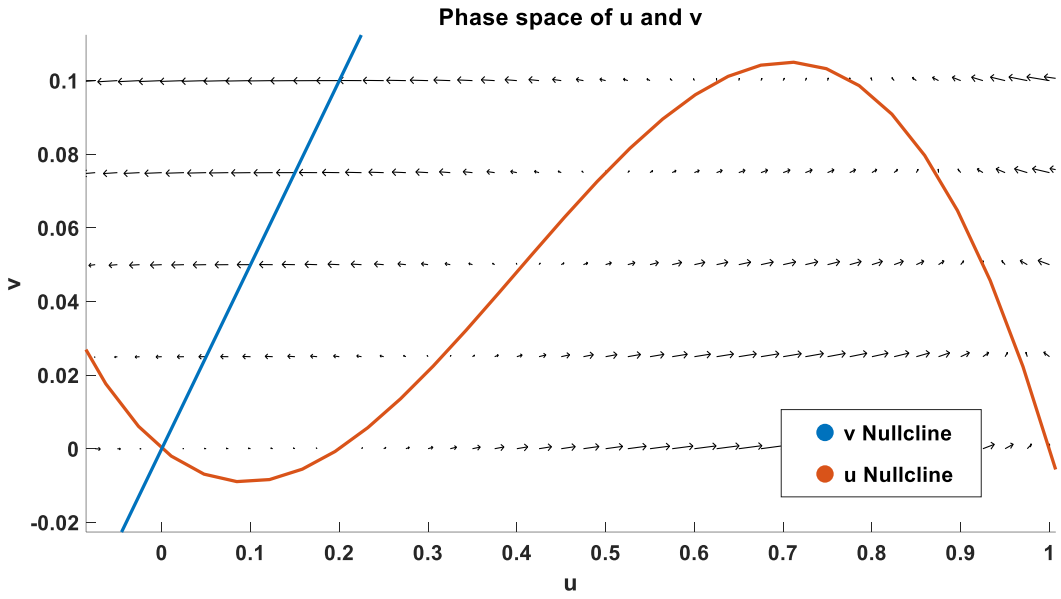

Figure 2 – FN phase space with nullclines and vector plot. Vector plot shows the system tends to approach the nullclines. $u_{rest} = 0$, $u_{threshold} = .2$, $u_{max} = 1$, $A = 1$ and $\beta = .5$.

Intersection of the u and v nullclines ($u = 0$ and $v = 0$) is a stable node in which the system will converge unless perturbed. Perturbing the system below the u nullcline (i.e., $u = 0.3$

and $v = 0$) and following the vector plot shows the system beginning an AP cycle with an upstroke approaching the u nullcline from the left. Once at the u nullcline, u quits increasing and v begins to increase inducing the excited phase of the AP cycle. Following the u nullcline, when the system reaches the top of the u nullcline, the value of u begins to decrease rapidly until reaching the u nullcline again from the right and following the u nullcline again. The system will slowly return to the stable node at $u = 0$ and $v = 0$. Assuming the initial conditions of $u(0) = 0$ and $v(0) = 0$, the system is solved numerically, with an instantaneous perturbation from J_{stim}, and it demonstrates how the phase space describes the dynamics of the FN system in Figure 3.

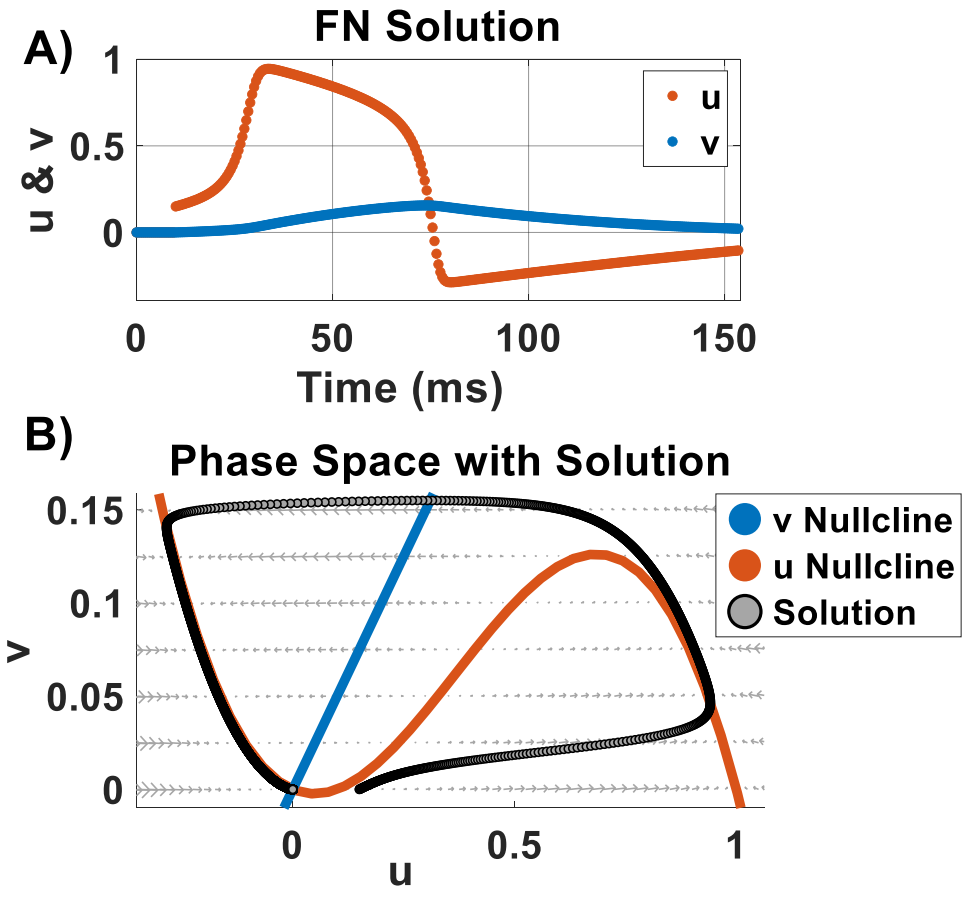

Figure 3 – FN solution and nullclines. Panel A shows the numerical solution to (11) and (12) as functions of time. Panel B shows u and v plotted against each other and overlapped over

the Figure 2 to demonstrate how the nullcline and vector plots describe the overall behavior of the FN model.

Overall FN is a simple model which describes the cellular dynamics of an excitable cell. The model demonstrates that a mathematical model may simulate the behavior of excitable cells.

Excitable cells are typically connected to each other through gap junctions or the extracellular matrix. The process of an excited cell stimulating surrounding cells may be simulated using a diffusive current. A diffusive current assumes that there is a flux of ions from one cell to another which changes the transmembrane potential of surrounding cells until surrounding cells become excited and propagate this behavior to next neighboring cells. Assuming that the conductivity of the extracellular matrix is equal to the conductivity of the interior of the cell, FN with a diffusive current is described by (15) and (16).

$$C_m \frac{\partial u}{\partial t} = \nabla \cdot \left(\widetilde{\mathrm{D}} \nabla u\right) - A(u - u_{rest})(u_{Excitable} - u)(1 - u) - v + J_{Stim} \quad \textbf{(15)}$$

$$\frac{\partial v}{\partial t} = \varepsilon(\beta u - v) \quad \textbf{(16)}$$

Applying the conditions that J_{Stim} excites the cell above a set threshold, $\widetilde{D}$ is homogeneous, the system is in a one dimensional cable, with the initial conditions $u(x, 0) = 0$ and $v(x, 0) = 0$ and the boundary conditions $\frac{\partial u(0,t)}{\partial x} = 0$ and $\frac{\partial u(L,t)}{\partial x} = 0$, (15) and (16) are numerically solvable and are shown in Figure 4.

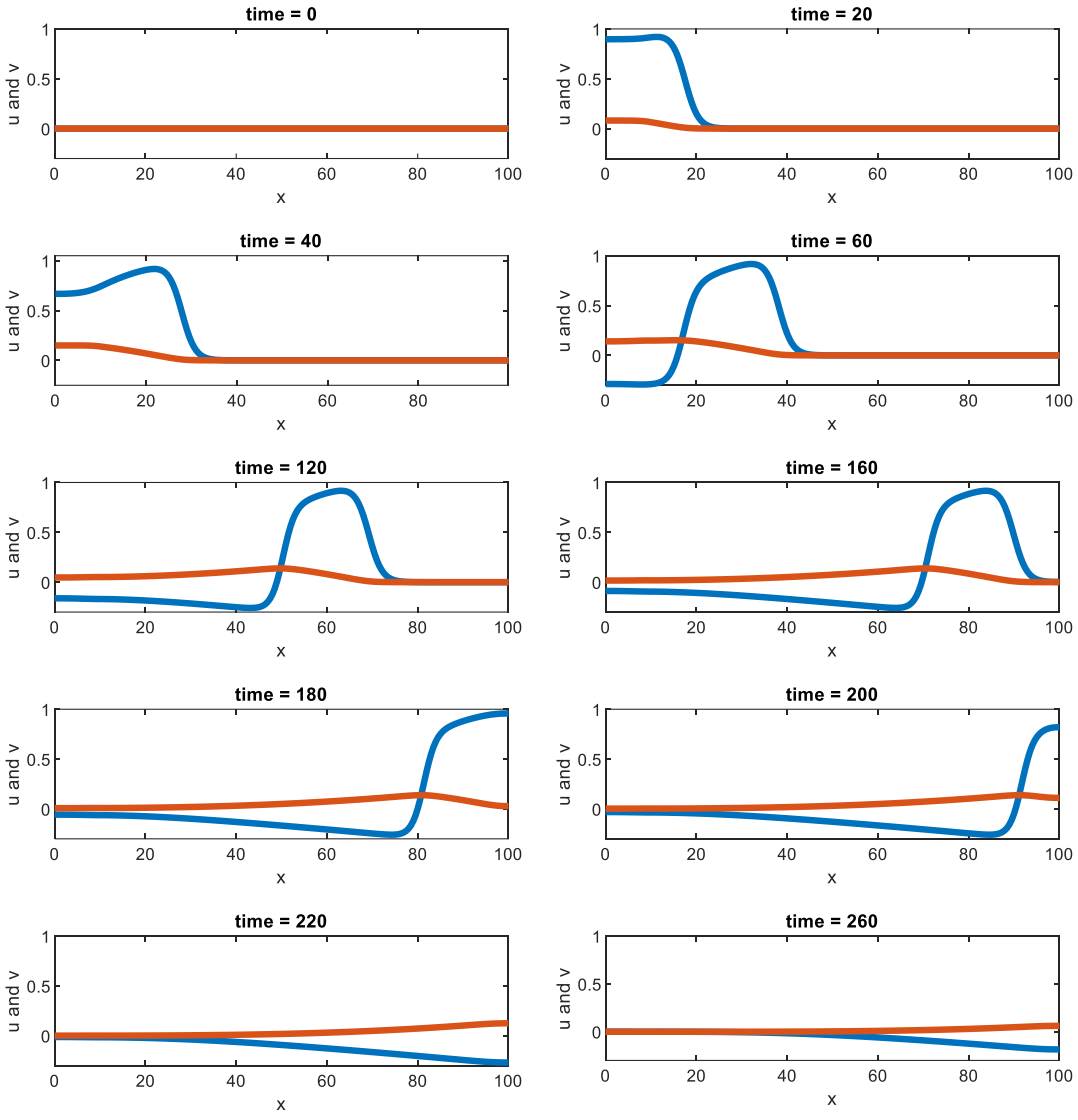

Figure 4 – Traveling FN wave. Excitation of the 1D cable occurred by applying a current between the positions 0 and 10 and occurred between time=0 and time =20. Propagation of wave continued and at time=60 appearance of the wave back of the reaction-diffusion wave. Wave propagation continues until it interacts with the boundary at x=100. Progression of system returning to rest is shown at time=220 and time=260.

Altogether FN model readily demonstrates the behavior of reaction-diffusion systems along with the traveling wave dynamics. More accurate models exist for cardiomyocytes, but all

follow the general behavior described by the FN model which includes a quick depolarization, an excited and repolarization phases.

Artificial Intelligence/Neural Networks

Artificial Intelligence (AI) is defined by Oxford dictionary as “the theory and development of computer systems able to perform tasks that normally require human intelligence, such as visual perception, speech recognition, decision-making, and translation between languages.”. Within AI there are subcategories, such as machine learning, which uses computer programs to improve their predictive ability based upon previous experience. Supervised learning is a machine learning task which uses labeled data to train a model. The data consists of inputs and targets/outputs. The goal of supervised learning is to train a model to recognize statistical patterns to correctly predict target outputs from inputs. Supervised learning can perform classification or regression predictions.

Neural networks are very popular and have recently become a standard algorithm among scientists. Neural networks are mathematical models which are designed to mimic the neuronal activity with the brain. The brain is composed of neurons which interconnect and process signals depending on the synaptic strength between neurons. When connected neurons fire more often the synaptic strength between them increases. In neural networks the synaptic strength is commonly referred to as a weight. In neural networks the neurons are considered nodes. In supervised learning when a feature within the input is detected a node is activated and will fire causing the connected nodes to activate. Within neural networks nodes are typically placed in layers with other nodes. These layers are interconnected to neighboring layers to mimic the connected neurons in the brain. Typically, all the nodes in a layer are connected to every node in

neighboring layers. A layer which is between the input and output layers are considered hidden layers. A general diagram is shown in Figure 5.

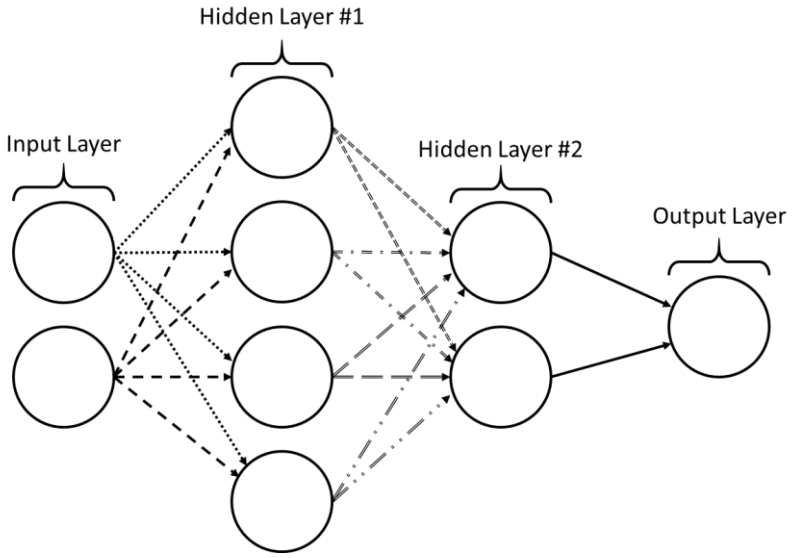

Figure 5 – Example of a general layout of a neural network.

In Figure 5 the input layer connects to Hidden Layer #1 using an activation function. An activation function is typically a function that takes an input and controls the connection strength to the next node. There are numerous types of activation function such as hyperbolic tangent, sigmoid, rectified linear unit (ReLU), step, linear, etc. The input of the activation functions are represented by linear functions where the previous nodes value is multiplied by the weight of the connection plus a bias. A bias is a linear shift to the input that causes the connection between nodes to be stronger or weaker. An example of input and activation is described by (17) and (18) using the notation that subscript k refers to the layer position.

$$z_{k-1} = w_{k-1} * A_{k-1} + b_{k-1} \quad \textbf{(17)}$$

$$A_k = a[z_{k-1}] \tag{18}$$

w_{k-1} are the weights connecting the nodes of layers k and $k-1$, A_{k-1} is the activation values of nodes of the pervious layer $k-1$, b_{k-1} is the bias connecting the nodes of layers k and $k-1$, a is any activation function used to activate nodes at layer k and A_k is the activation values of the nodes at layer k. The activation process continues through all the layers, using the previous layers activation values, until the output layer is calculated. This process is called a forward pass. The calculated output layer activation values, from a forward pass, are called the predicted outputs and are denoted $\hat{y}$.

Training

To determine the optimal values of the weights and biases, neural networks are trained. Training uses a process called back propagation to update the weights and biases within the network one layer at a time from the output layer to the input layer. All the initial values of the weights are determined stochastically from a random number generator and the biases are typically initialized to zero. Completing a forward pass, predicted outputs are obtained and a loss function is used to determine the difference between the predicted and target outputs. There are multiple types of loss functions such as mean absolute error, mean squared error, cross entropy, etc. Using the loss function and differential calculus, the weights and biases can be updated using back propagation. Back propagation allows for gradient descent in which the weights and biases are changed until the loss function is minimized. For updating the last hidden layer of a neural network (denoted n), this process is described by (19)-(22).

$$loss = \mathrm{L} = g[y - \hat{y}] \tag{19}$$

$$\frac{\partial L}{\partial w_{n-1}} = \frac{\partial L}{\partial \hat{y}} \frac{\partial \hat{y}}{\partial z_{n-1}} \frac{\partial z_{n-1}}{\partial w_{n-1}} \tag{20}$$

$$\frac{\partial L}{\partial b_{n-1}} = \frac{\partial L}{\partial \hat{y}} \frac{\partial \hat{y}}{\partial z_{n-1}} \frac{\partial z_{n-1}}{\partial b_{n-1}} \tag{21}$$

$$\frac{\partial L}{\partial A_{n-1}} = \frac{\partial L}{\partial \hat{y}} \frac{\partial \hat{y}}{\partial z_{n-1}} \frac{\partial z_{n-1}}{\partial A_{n-1}} \tag{22}$$

Using the values obtained from the forward pass, (19)-(22) can be calculated numerically. The weights and biases can be adjusted by (23) and (24).

$$dw_{n-1} = -\alpha \frac{\partial L}{\partial w_{n-1}} \tag{23}$$

$$db_{n-1} = -\alpha \frac{\partial L}{\partial b_{n-1}} \tag{24}$$

α is a learning rate which adjusts the rate of change of the weights and biases. Learning rates can be static or variable. A learning rate which is neither too high or low is used to converge to the optimal weight and bias values without “overshooting” or converging too slowly. A learning rate which is too high will not converge to an optimal weight and bias values.

Backpropagation occurs through each hidden layer of the neural network starting from the last hidden layer to the first. In reference to (19)-(22), the next layers in the back propagation is updated by (25)-(27).

$$\frac{\partial L}{\partial w_{n-2}} = \frac{\partial L}{\partial \hat{y}} \frac{\partial \hat{y}}{\partial z_{n-1}} \frac{\partial z_{n-1}}{\partial A_{n-1}} \frac{\partial A_{n-2}}{\partial z_{n-2}} \frac{\partial z_{n-2}}{\partial w_{n-2}} = \frac{\partial L}{\partial A_{n-1}} \frac{\partial A_{n-2}}{\partial z_{n-2}} \frac{\partial z_{n-2}}{\partial w_{n-2}} \quad \textbf{(25)}$$

$$\frac{\partial L}{\partial b_{n-2}} = \frac{\partial L}{\partial \hat{y}} \frac{\partial \hat{y}}{\partial z_{n-1}} \frac{\partial z_{n-1}}{\partial A_{n-1}} \frac{\partial A_{n-2}}{\partial z_{n-2}} \frac{\partial z_{n-2}}{\partial b_{n-2}} = \frac{\partial L}{\partial A_{n-1}} \frac{\partial A_{n-2}}{\partial z_{n-2}} \frac{\partial z_{n-2}}{\partial b_{n-2}} \quad \textbf{(26)}$$

$$\frac{\partial L}{\partial A_{n-2}} = \frac{\partial L}{\partial \hat{y}} \frac{\partial \hat{y}}{\partial z_{n-1}} \frac{\partial z_{n-1}}{\partial A_{n-1}} \frac{\partial A_{n-1}}{\partial z_{n-2}} \frac{\partial z_{n-2}}{\partial A_{n-2}} = \frac{\partial L}{\partial A_{n-1}} \frac{\partial A_{n-2}}{\partial z_{n-2}} \frac{\partial z_{n-2}}{\partial A_{n-2}} \quad \textbf{(27)}$$

Similar to (23) and (24), the weights and biases are updated at layer $n-2$ by (28) and (29).

$$dw_{n-2} = -\alpha \frac{\partial L}{\partial w_{n-2}} \quad \textbf{(28)}$$

$$db_{n-2} = -\alpha \frac{\partial L}{\partial b_{n-2}} \quad \textbf{(29)}$$

Continuing with more layers, a recursive pattern emerges where the next layer, propagating backwards, has the previous layers change in loss with respect to the previous layers' change in activation. Noting the recursive piece of (25)-(29), the general formula for updating the weights and biases of any layer are defined by (30)-(34).

$$\frac{\partial L}{\partial w_{i-1}} = \frac{\partial L}{\partial A_i} \frac{\partial A_{i-1}}{\partial z_{i-1}} \frac{\partial z_{i-1}}{\partial w_{i-1}} \quad \textbf{(30)}$$

$$\frac{\partial L}{\partial b_{i-1}} = \frac{\partial L}{\partial A_i} \frac{\partial A_{i-1}}{\partial z_{i-1}} \frac{\partial z_{i-1}}{\partial b_{i-1}} \quad \textbf{(31)}$$

$$\frac{\partial L}{\partial A_{i-1}} = \frac{\partial L}{\partial A_i} \frac{\partial A_{i-1}}{\partial z_{i-1}} \frac{\partial z_{i-1}}{\partial A_{i-1}} \quad \textbf{(32)}$$

$$dw_{i-1} = -\alpha \frac{\partial L}{\partial w_{i-1}} \quad \textbf{(33)}$$

$$db_{i-1} = -\alpha \frac{\partial L}{\partial b_{i-1}} \quad \textbf{(34)}$$

(30)-(34) show the backpropagation method which updates all the weights in a neural network one layer at a time and stopping at the first hidden layer in the neural network.

The weights and biases are adjusted through repeating the process of forward pass, calculate the loss function and updating the weights and biases using backpropagation. Backpropagation can either be performed on each instance individually or may be performed on a sum of multiple instances at a time called a batch. Each occurrence of updating using backpropagation on the entire test set is defined as an epoch. The process continues until the loss function passes a threshold of epochs or until the change in loss with respect to previous epochs stops decreasing.

When the training process is completed, the neural network can be assessed using different statistical analysis. For classification the metrics are typically include accuracy, specificity, precision, recall, Receiver Operating Characteristic (ROC), etc. In a regression model the metrics are typically reported as mean square error (MSE), normalized root MSE (NRMSE), Coefficient of Determination or r^2, calibration curves, etc[13].

Convolutional Layers

Convolutional neural networks (CNN) are neural network with convolutional layers which contain filters to extract data from multidimensional images. In this section we will discuss the one-dimensional (1D) cases in which the multidimensional image is assumed to be a 1D signal. Filters are vectors, made up of randomly distributed weights, which overlap the signal

to extract the features of the signal. Moving over the signal at a set stride length, the filter is convoluted at each step length of the signal. The more similar the filter is with the signal the higher the value of the convolution. The output of a convolutional layer is a vector containing all the convolutions over the signal. This process is visualized in Figure 6.

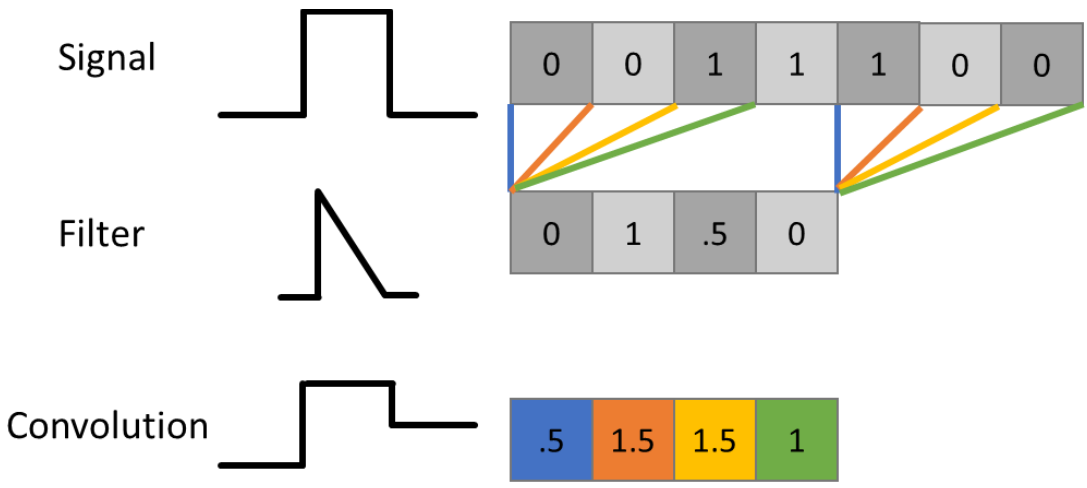

Figure 6 – Visual description of convolution between signal and filter. Dot product occurs between each stride which is represented by each paired color lines and corresponds to the output vector value of the same color.

The output of a convolution is then passed through an activation function, where each element of the convolution is treated as a node, and is typically connected to a dense neural layer, like Figure 5, to complete the neural network. The filters are updated using backpropagation of error where the filter values are the weights and are updated in a similar fashion in the training section. Each convolutional layer uses multiple filters in the same manner, and each have their own output vector which is passed to the next layer after being activated by an activation function.

A common technique on convolutional layer outputs is to reduce the data size using a pooling layer. A pooling layer will group the output data in a set range. The most common approach is to take the max value in a range. The max value is assumed to represent the entire range. An example of max pooling is shown in Figure 7.

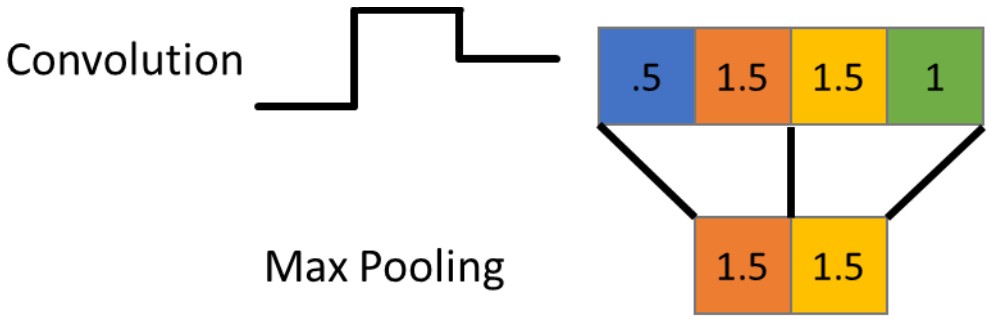

Figure 7 – Max pooling of a convolutional layer. The pool size is 2.

Long-Short Term Memory Layers

Long-Short Term Memory (LSTM) layers are a type of recurrent layer in which the input vector is operated upon each time step independently. Information from a previous cell is passed to the next cell which allows the layer to handle temporal data. Compared to a recurrent layer, an LSTM cell includes a memory gate to manage the vanishing gradient problem. The vanishing gradient problem occurs during backpropagation when a neural network has many layers and the weights of layers further from the output layer are not updated because the gradient of the loss function has diminished due to the nature of backpropagation from too many previous layers. This effect is enhanced in a recurrent neural network because each time step uses backpropagation of error. LSTM uses a memory gate to prevent the effects of the vanishing gradient problem. Memory gates use the previous LSTM cells' outputs to control how much the

weights and memory gates in the current LSTM cell can change. This offsets the vanishing gradients effect and allows proper training of the neural network. An LSTM cell is described in Figure 8.

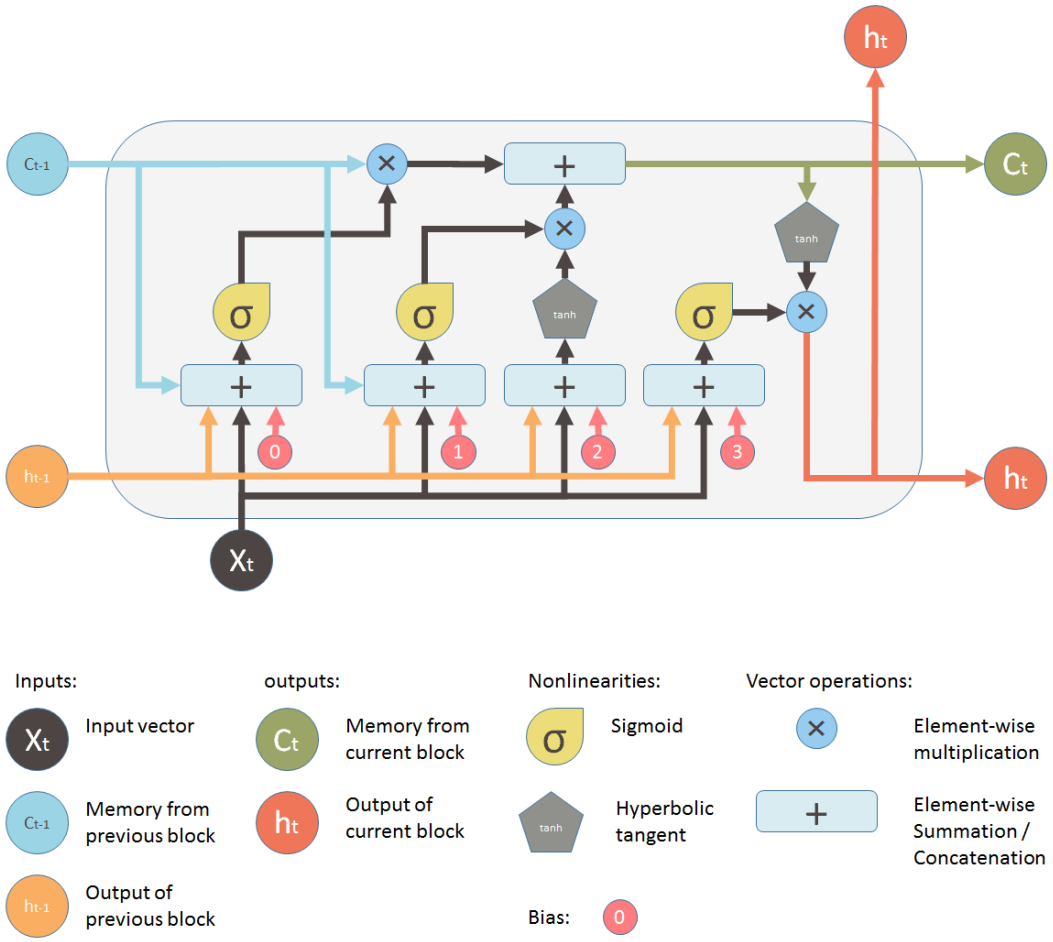

Figure 8 – Description of LSTM cell. The Cell uses the previous LSTM cells output and state/memory to predict the current LSTM cells' output and cell state/memory. Reproduced from Yan [14]

Overall LSTM neural networks can handle temporal data in a manner that allows proper training of the neural network. LSTM and convolutional layers can be used within the same

neural network, denoted as a CNN-LSTM neural network, to predict outputs from temporally discrete image data.

Goals

The overall hypothesis of this dissertation is that simplified 2D and 3D models of the left ventricle can provide valuable information for theoretically detecting or predicting myocardial ischemia within the human heart. Data collected from these models can be analyzed using traditional and deep learning methods to prevent severe ischemic diseases.

The goals of this dissertation are as follows,

1. Determine key characteristics of 2D ventricle model to determine transmural ischemic growth.
2. Apply deep learning convolutional neural network to 3D ventricle model data to determine the volume and severity from ECG signals.
3. Apply deep learning regression methods to 3D ventricle time series data to predict the future state of myocardial ischemia.

CHAPTER II: EVALUATION OF SEVERITY OF CARDIAC ISCHEMIA USING *IN SILICO* ECG COMPUTED FROM 2D REACTION DIFFUSION MODEL[15]

Abstract

This study focuses on the analysis of the bioelectrical activity of the left ventricle using a 2D Bueno-Orovio-Fenton-Cherry monodomain reaction diffusion model. ECGs signals are simulated for normal and ischemic conditions of varying severity. Changes in ischemia are examined in a single precordial lead as the size of the ischemic area increases in various locations. Analyzing this single lead ECG, we determine the ratio between ST deviation and T-wave amplitude and establish a threshold sufficient for monitoring acute ischemic event. This method may be potentially implemented to predict sudden cardiac death.

Introduction

Among all causes of mortality cardiovascular disease (CVD) ranks near the top representing 31% of all global deaths and amounts to 17.9 million people who died from CVD in 2016 [16]. The CVD, which is an occlusion of coronary arteries, often results in a deficiency of oxygen supply known as cardiac ischemia. Acute form of this disorder poses a significant danger since it may frequently result in heart attack and cardiac death.

A common approach to predict the development of cardiac ischemia is tracking a body surface electrocardiogram (ECG). Using the forward problem of electrocardiology [17], a body surface ECG may be simulated utilizing reaction diffusion (RD) equations which describe ionic processes inside a myocardium. The reaction part of these equations characterizes the flow of ions through cellular membrane channels. The diffusion part describes the diffusive flow of charges between the neighboring cellular membranes. Cumulatively, these processes determine

the dynamics of cellular transmembrane potentials (action potential, AP) and ascertain the magnitude of electric field of the heart induced at the surface of the body.

Our approach is centered on numerical simulations of body surface ECGs signals by using the RD models with simplified geometries. Though detailed 3D models are commonly preferred[18], the simplified 2D models have also been proved to provide valuable information by keeping intact fundamental features of excitation in normal and ischemic myocardium[19].

It is well known that myocardial ischemia raises cellular membrane resting potential, shortened AP duration and decreases the AP upstroke velocities [20,21]. In turn, these changes affect the surface ECG by shifting its baseline voltage and altering the morphology of the ST segment, QRS complex and T-wave. We will study *in silico* ECG signals computed from the 2D reaction-diffusion model and will evaluate the severity of cardiac ischemia for various model parameters.

Methods

Model Geometry

For the average adult male, the distance from the center of the base of the Left Ventricle (LV) to its inner wall is ~ 2 cm. It is shorter than the distance from the LV base to the inner wall of the apex ~ 6 cm. Generally, the myocardial thickness varies from ~1 cm at the base to ~ 2 cm at the apex. Using these dimensions, the coronal cross section of the LV may be approximated as a 2D symmetric horseshoe (Figure 9). The horseshoe is made of two concentric ellipses with the same axes. The inner and outer ellipses have semi-major and semi-minor axis of 6 and 2 cm and 8 and 3 cm, respectively. Using these proportions, the following coordinate system can be utilized to approximate the coronal cross section of LV ((35) and (36)).

$$a = \sqrt{x^2 + \frac{y^2}{s^2}} \tag{35}$$

$$\theta = arctan\left(\frac{y}{sx}\right) \tag{36}$$

Here, *x* and *y* are the Cartesian coordinates and s is the scaling value to fit two concentric ellipses with different semi-major and semi-minor axes lengths. Parameter *s* is the slope of the regression line "$y = sx$", which is equal to 2.796 ($R^2 = .84$). Such fitting corresponds to semi-minor axis of 2 and 3 cm and to semi-major axis of 5.54 and 8.30cm, respectively (Figure 9).

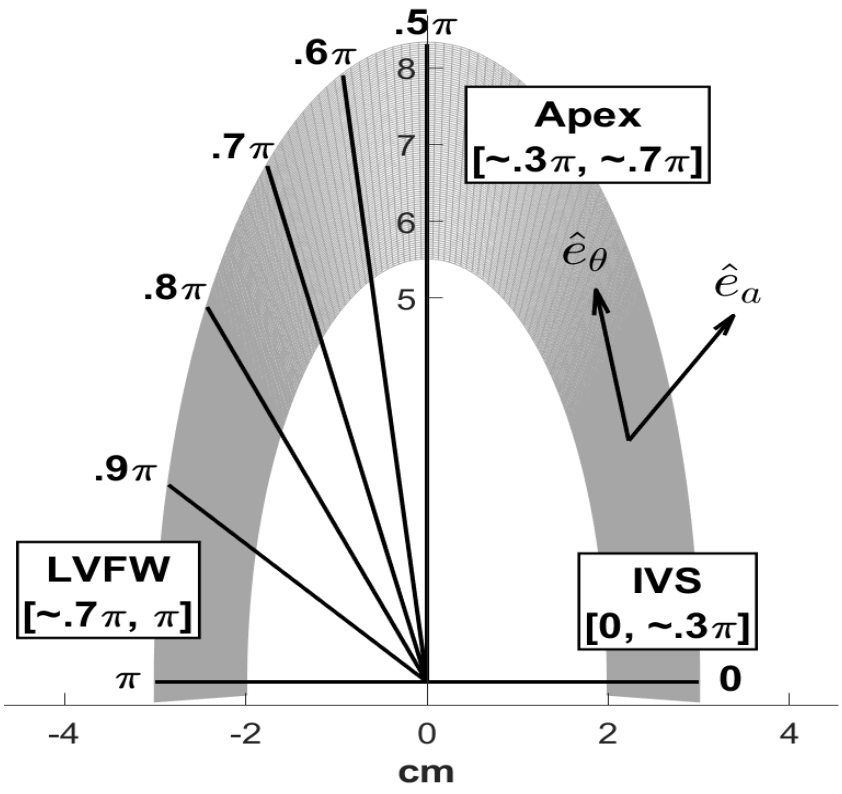

Figure 9 - Horseshoe model geometry in a non-orthogonal basis ($\hat{e}_a, \hat{e}_\theta$). Intraventricular septum (IVS) and left ventricular free wall (LVFW) are located between angles θ varying from 0 to 0.3π and from 0.7π to π, respectively. The apex is located between IVS and LVFW. LVFW is divided at specific points θ= [0.5π,0.6π,0.7π,0.8π,0.9π, π].

Using coordinate system ((35) and (36)) we generated a finite difference (FD) mesh with constant Δa (0.01 cm) and $\Delta\theta$ (0.01π) mesh intervals, which spanned from 2 to 3 cm and from 0 to π radians, respectively.

Reaction Diffusion Model and Equations

Simulations were done using the Bueno-Orovio-Fenton-Cherry reaction diffusion model (BOFC) [22]. The main part of the RD BOFC model which includes isotropic diffusion and the Laplacian for the spatial coordinates described in (36) is defined by (37).

$$\frac{\partial u}{\partial t} = D\left(\left(\cos^2\theta + \frac{\sin^2\theta}{s^2}\right)\frac{\partial^2 u}{\partial a^2} + \left(-\sin 2\theta\,\frac{(s^2-1)}{a\ s^2}\right)\left(\frac{\partial^2 u}{\partial a\partial\theta} - \frac{1}{a}\frac{\partial u}{\partial\theta}\right)\right. \quad \textbf{(37)}$$

$$\left. + \left(\frac{\cos^2\theta + s^2\sin^2\theta}{(a\ s)^2}\right)\left(\frac{\partial^2 u}{\partial\theta^2} - a\frac{\partial u}{\partial a}\right)\right) - \sum_{i=fo,so,si} J_i(v,w,s)$$

$$+ J_{Sim}$$

Here u is a dimensionless variable which denotes a transmembrane potential. The magnitude of diffusion was set to $D = 4.7\ cm^2/sec$. Values of J_i represent the membrane ionic currents [22]. J_{Stim} indicates the stimulus current that excites the cells (see section 3.1). No flux Neumann boundary conditions were used in the direction normal to all the boundaries of the horseshoe geometry.

Myocyte cells APs include high depolarization and low repolarization rates. We reproduced this behavior in all different parts of the LV including epicardial, endocardial and mid-myocardial zones. BOFC parameters were set in the way to reflect these changes within epicardial, and endocardial cells APs are normally shorter than in mid-myocardial cells (Figure 10).

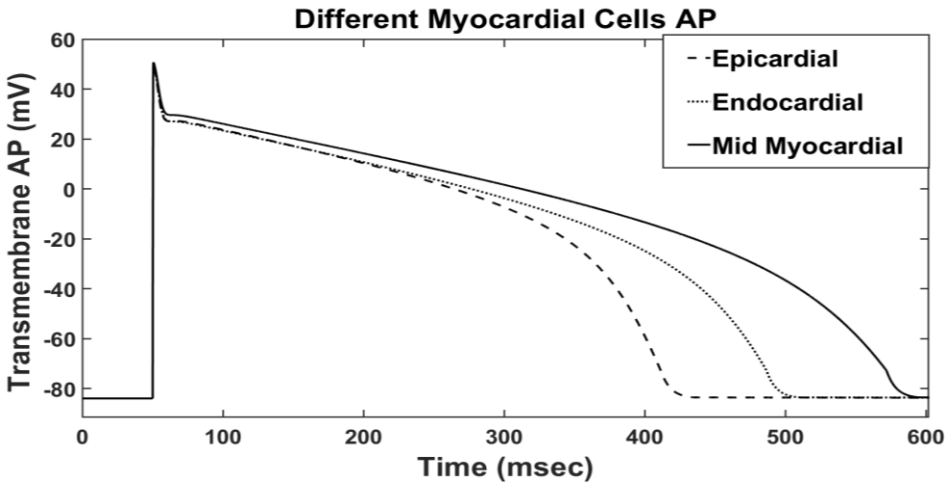

Figure 10 - APs for different cell types. Dashed black line represents an epicardial cell AP, dotted gray line denotes an endocardial cell AP and solid black line represents a mid-myocardial cell AP.

Simulating ECG

Body surface ECG signals are calculated using Maxwell, Poisson, and continuity equations [17]. By assuming the thorax as an infinite homogeneous conductor, the *in silico* ECG can be calculated at the body surface electrode using (38).

$$ECG(t) = \iiint_{\tau} \frac{D\nabla V_m \cdot \vec{r}}{|r|^3} d\tau \qquad \textbf{(38)}$$

Where *D* is the diffusive tensor, V_m is the transmembrane potential, r is the position between the electrode and the point where V_m is measured in the medium, and $d\tau$ is the volume scaling factor. In our case the volume integral (38) was replaced with the area integral and was computed using trapezoidal method every 0.7 msec.

The diffusive currents that wrap around the LV in a direction perpendicular to $\hat{e}_a$ and $\hat{e}_\theta$ (denoted as $\hat{e}_\phi$) are symmetric and are approximately perpendicular to a recording electrode (RE) placed outward from the apex in the direction approximately corresponding to precordial lead V4. Therefore, the $\hat{e}_\phi$ diffusive current is much less than diffusive currents in the directions $\hat{e}_a$ and $\hat{e}_\theta$.

Results

Propagation in the 2D model

The excitation which is initiated by a stimulus current J_{Stim} raises the transmembrane potential above a threshold starting an AP sequence. We used a traveling J_{Stim} that started at $\theta = 0.25\pi$ and ended at $\theta = 0.9\pi$ with the excitation range $a = 2.05 - 2.17\ cm$ and $\theta \pm 0.01\pi$, respectively. Velocity of the J_{Stim} excitation wave was equal to $4\frac{m}{s}$.

All simulations were performed by implementing the second order spatial finite difference method (FDM) and the first order temporal FDM.

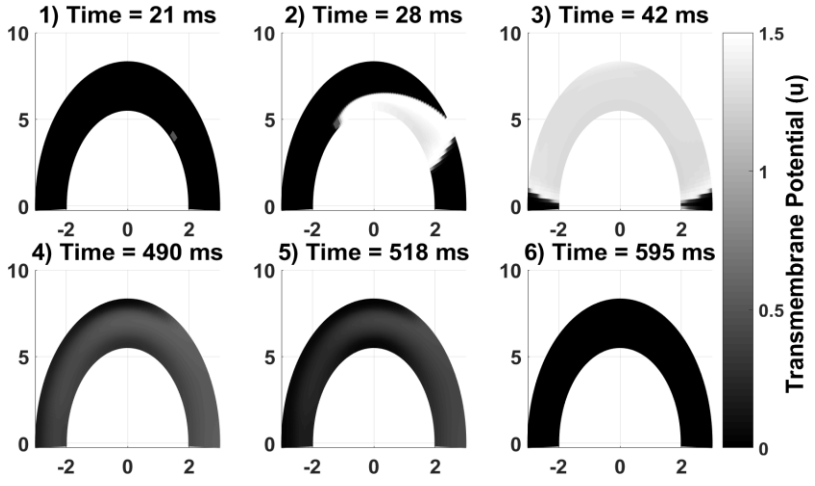

Figure 11 - Propagation of the excitation within the 2D horseshoe model in Cartesian coordinates. Panel 1 shows J_{Stim} initial excitation of the medium at $\theta = 0.25\pi$ and $a = 2.2$, which initiates the wave front shown by the light grey changing to black boundary.

Panel 2 shows J_{Stim} quickly depolarizing the LV at a constant $a = 2.2\ cm$ and moving in the positive θ direction while the wave front continues to propagate at a slower speed outward from where J_{Stim} has originally excited the myocardium. Panel 3 shows J_{Stim} stopping at $\theta = 0.9\pi$. Panel 4 shows the wave back starting in the epicardium before the endocardium and mid-myocardium; wave back is denoted as the area in transition from the black to the grey region. Panel 5 shows 2 wave backs propagating from endocardium and epicardium towards the mid-myocardium. Panel 6 shows the entire medium returning to resting potential.

Normal ECG

Using the baseline parameters mentioned in Reaction Diffusion Model and Equations, (37) and (38) were solved under normal non-ischemic conditions. The RE was placed at $r = (0, 10, 0)$ and the evolution of excitation was like that shown in Figure 11. A typical normal body surface ECG signal is depicted in Figure 12.

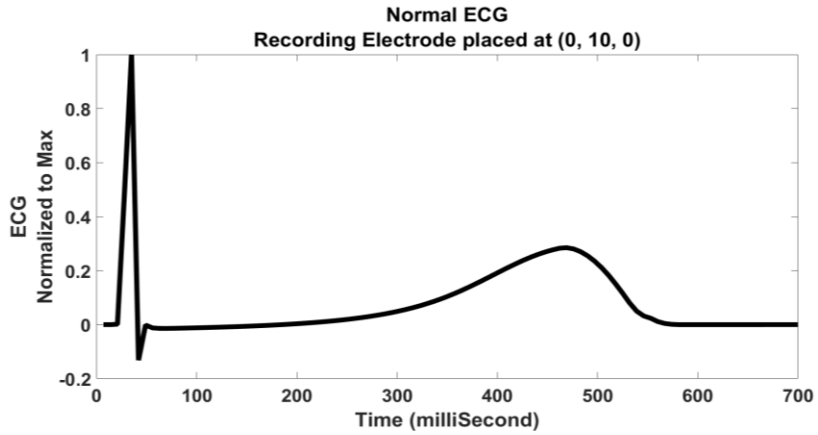

Figure 12 - Normal ECG from the 2D model in Figure 9. The RE is placed at $r = (0, 10, 0)$. The key feature of the normal left ventricle ECG is characterized by a tall and narrow QRS complex and a relatively low amplitude and broad T-wave. The Q wave in Figure 12 is absent since only the left ventricle is being considered.

Transmural myocardial infarction (MI)

We modeled ischemic myocardium by elevating the parameter u_o, which controls the cellular resting potential (RP), in a certain area of myocardium. Typically, ischemia starts in the endocardium and expands outwards rapidly towards the epicardium [23]. To represent this growth at different regions of our horseshoe model, the width was centered and varied in the range of $\theta = [0.5\pi, 0.6\pi, 0.7\pi, 0.8\pi, 0.9\pi, \pi] \pm 0.05\pi$ radians. The ischemic area for all θ increased in the $\hat{e}_a$ direction from $a = 2$ (endocardium) to $a = 3$ (epicardium). The ischemic ECG signals were computed for the different angles within the range indicated above.

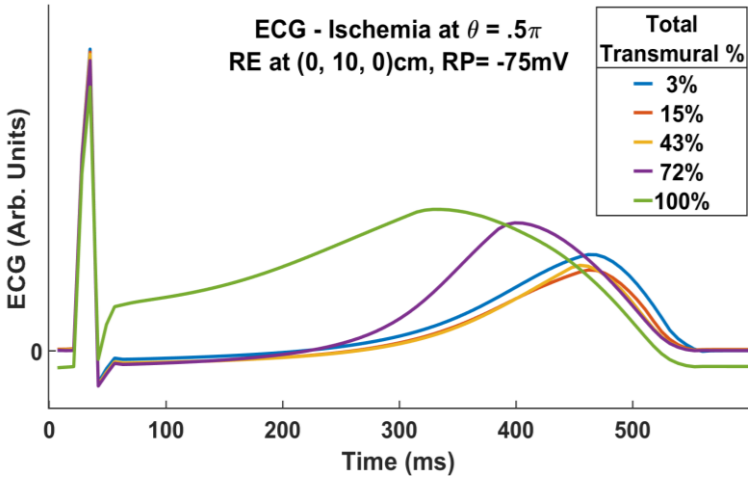

Figure 13 - ECGs computed by increasing the ischemic area at $\theta = 0.5\pi$. Blue curve (3%) is practically a normal ECG (Figure 12) and green curve represents a transmural MI.

Similar simulations were done at the other angular positions described above. The value of u_o was increased to .1 (-75 mV) in ischemic area for all simulations. We observed that the ratio between ST deviation and T-wave amplitude (γ) did not change significantly with ischemic area for ischemic center locations confined at the higher angles θ greater than 0.7π. On the contrary, at $\theta < 0.7\pi$ we noted a sharp increase in γ for ischemic areas greater than ~1.4cm^2.

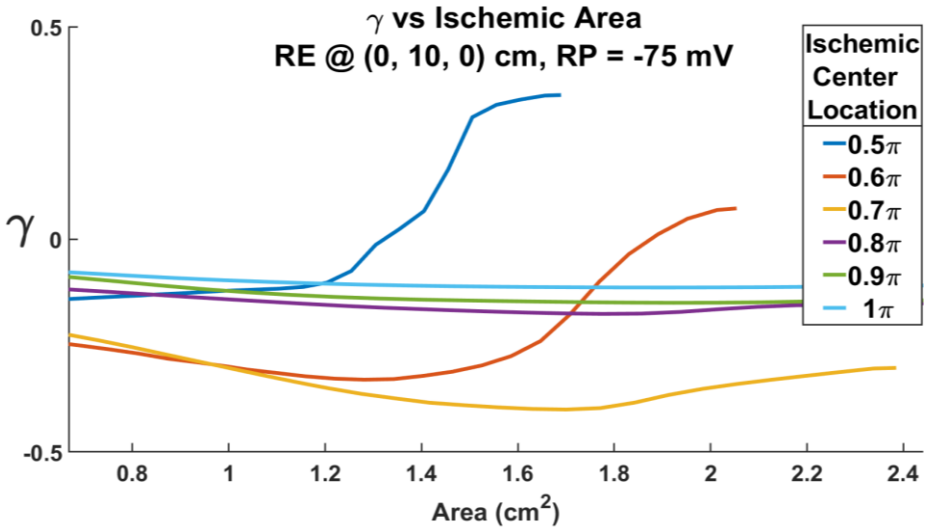

Figure 14 - Dependence of γ on the magnitude of ischemic area. Curves represent endocardium to epicardium growth at different locations in the LV apex and the LVFW. Legends show locations of the ischemic area center position. ST deviation was calculated as the ECG amplitude at the J_{60} point. The end of every curve designates the states of fully developed transmural ischemia designated as MI.

Calculated Severity of Ischemia

Severity of ischemia was defined as the rate of changes in ischemic area per unit time (39).

$$Severity \equiv \frac{\partial Area}{\partial t} = \frac{\partial \text{Area}}{\partial \gamma}\frac{\partial \gamma}{\partial t} \quad \textbf{(39)}$$

The rate of changes in γ per unit ischemic area can be recalculated from data shown in Figure 15.

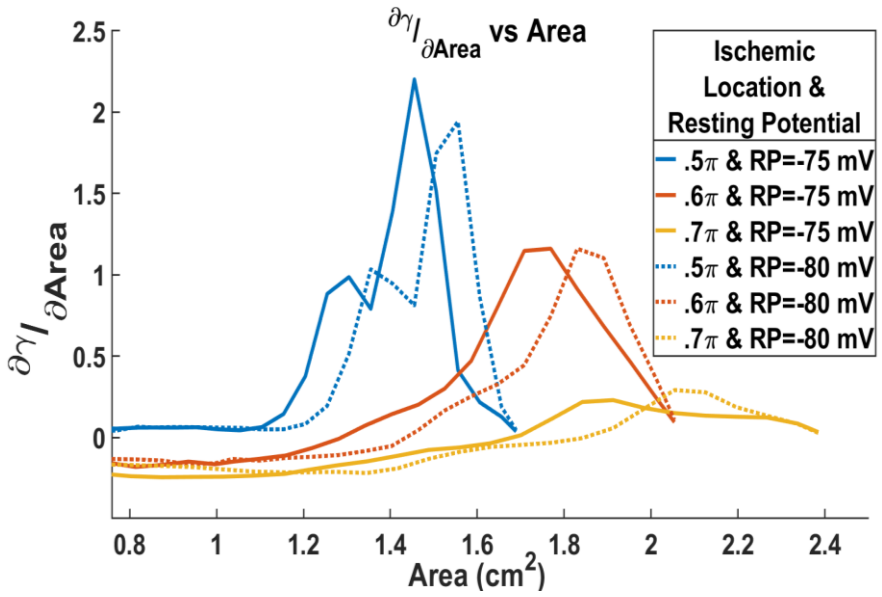

Figure 15 - Changes in γ per unit ischemic area are depicted for different ischemic growth at different angles θ. The signals recorded at $\theta = 0.5\pi$ and 0.6π demonstrate sharp changes like those shown in Figure 14.

A coefficient $\left(\frac{\partial\gamma}{\partial\text{Area}}\right)^{-1}$ (see Figure 15) can be considered in conjunction with another coefficient $\frac{\partial\gamma}{\partial t}$ determined from the original V_4-type ECG signal. Combined these coefficients can be used for the estimates of severity of ischemia. Specifically, the average half maximum value of the $.5\pi$ curves in Figure 15 ($A = 1.04\ cm^{-2}$) is a sufficiently accurate threshold to designate the fastest, and consequently the most dangerous ischemic growth.

Discussion

We demonstrated that it is possible to quantify the rate of ischemic growth using a single precordial lead aligned with the $\hat{e}_\theta$ direction in a 2D model of myocardium. Using $(A)^{-1}$ instead of the $\frac{\partial\text{Area}}{\partial\gamma}$ in (39) one can calculate a critical value of $\frac{\partial\gamma}{\partial\text{t}}$. For instance, if the thickness of the myocardium is 1cm and ischemic area extends in the $\hat{e}_\theta$ direction by 2 cm then the value of $\frac{\partial\gamma}{\partial\text{t}}$

may become greater than $0.018\ \mathrm{min}^{-1}$ indicating a quick spread of ischemia typical for the MI like ischemic event.

Finally, our model can be used in conjunction with machine learning to better understand more complex ischemic events.

Conclusions

Overall, we implemented a 2D reaction diffusion model to simulate the propagation of electrical excitation in the ischemic myocardium. It has been determined that the growth of the ischemic area results in increasing of the ratio γ. We found that the maximum $\frac{\partial \gamma}{\partial \mathrm{Area}}$ value of $2.25\ cm^{-2}$ indicates the strongest progression of the ischemic area. The critical (alert) value can be used to predict severe MI like ischemic growth if the value of $\frac{\partial \gamma}{\partial \mathrm{t}}$ is greater than $0.183\ min^{-1}$.

CHAPTER III: REACTION-DIFFUSION INFORMED APPROACH TO DETERMINE MYOCARDIAL ISCHEMIA USING STOCHASTIC *IN SILICO* ECGS AND CNNS[24]

Abstract

Every year, nine million people die globally from ischemic heart disease (IHD). There are many methods of early detection of IHD which can help prevent death, but few are able to determine the configuration and severity of this disease. Our study aims to determine the severity and configuration of ischemic zones by implementing the reaction-diffusion analysis of cardiac excitation in a model of the left ventricle of the human heart. Initially, this model is applied to compute twenty thousand *in silico* ECG signals with stochastic distribution of ischemic parameters. Furthermore, generated data is effectively ($r^2 = 0.85$) implemented for training a one-dimensional convolutional neural network to determine the severity and configuration of ischemia using only two lead surface ECG. Our results readily demonstrate that using a minimally configured portable ECG system can be instrumental for monitoring IHD and allowing early tracking of acute ischemic events.

Introduction

According to the World Health Organization, 17.3 million people around the world die every year due to heart disease. Ischemic heart disease (ischemia for short) is a major contributor to these deaths[25,26]. Ischemia is when oxygenated blood is unable to reach the myocardium, which causes the myocardial cells to die. When ischemia goes undetected it can lead to myocardial infarction (commonly referred to as a heart attack or MI). When an MI occurs, there is a "golden hour" in which a person is more likely to survive if they receive treatment quickly after the onset of an acute MI [27]. Detection of ischemic events is still a challenge in

electrocardiology. Early detection of ischemic events could improve and prevent death caused by ischemic events.

Currently there is very limited work that involves the preemptive detection of ischemic events. Typically, when ischemia is suspected, there are only a few tests (Electrocardiograms (ECGs), nuclear imaging, CT scans, blood tests, etc.) available to confirm it. However, these tests are typically performed using specialized instruments in a controlled setting. Ischemia can be silent where there are no ischemic symptoms and is sometimes only noticed after an MI. A simple device that is versatile, inexpensive and can determine early stages of ischemia could help to reduce the number of deaths due to heart disease.

Previous research to determine ischemia has mostly focused on studies of abnormalities in body surface ECG signals. These studies typically use 12 lead ECG and compare the differences between electrocardiographic leads to determine the general location and size of ischemic zones [28,29]. However, the use of *in silico* ECGs to determine the location of ischemia is limited and focuses predominantly on evaluation of bulk ischemic sizes (small, medium, large) considered only in specific discrete placements [30].

Based upon Helmholtz reciprocal principle, the bioelectrical current produced by the heart can be determined using an ECG lead which uses two electrodes as a source and a sink of charge [31,32]. By inducing a potential difference between the two electrodes, it is possible to observe the heart's bioelectrical currents that are in alignment with the ECG lead. This procedure is known as the forward problem of electrocardiology. The reverse of the forward problem is the inverse problem of electrocardiology, which is associated with certain constraints (regularization procedures) upon the ECG to provide information about the bioelectrical activity of the heart[17,33].

Common constraints placed on the inverse problem are solving only for epicardial potentials, which would not provide information about the remaining portion of the myocardium.

An alternative approach to regularization for the inverse problem of electrocardiology is in using artificial intelligence. Previous research tends to use the MIT-BIH database [34] which contains multi-lead ECGs that have been annotated by clinicians with different heart conditions [35–39]. The body surface ECGs are processed for data extraction or used as a time series signal to be implemented in an artificial intelligence framework to determine heart diseases. The signals are suitable for the analysis with a one- or two-dimensional convolutional neural network (CNN) which use kernels to convolute with ECG signals to extract the key ECG topological features and predict cardiac conditions. CNNs, like any other neural network, need a significant volume of input data to be properly trained. The MIT-BIH database does not contain ECG signals with corresponding ischemic information, such as configuration and severity. Currently, no such large database with this data exists.

To avoid the methodological challenges of the inverse problem, we introduce a simplified model of the hearts' left ventricle to generate *in silico* ECG signals suitable for training a CNN. In general, the left ventricle is shaped like an ellipsoid. The long axis length, from base to apex, is typically reported from 7.5 to 9.5 cm in diastole and the inner and outer diameter at the base is approximately 4 and 6 cm, respectively [40–42]. The thickness of the muscle is approximately 1cm through the entire left ventricle with some small variations. The ratio in mass of the left to right ventricle is approximately 2.5:1 [43]. Using previously determined values the mean volume of the left ventricular myocardium is 105mL [44,45]. Compared to the right ventricle, the left ventricle produces a noticeably greater amount of bioelectrical activity due to the larger mass. Using only

the left ventricle can give significant ischemic information as ischemia rarely occurs in the right ventricle alone [7,8,46].

In summary, we propose to implement an *in silico* reaction-diffusion (RD) model to compute the data necessary to train a one-dimensional (1D) CNN via regression to determine the configuration and severity of ischemia within the left ventricle.

Method

Three-Dimensional Modeling

To describe the propagation of electrical excitation in the *in silico* model of the hearts' left ventricle we consider RD equations defined in the skewed spherical coordinate system. These coordinates are an extension to the two-dimensional coordinates used in our previous work [15]. The skewed spherical coordinates are described in (40)-(42).

$$x = a\,Cos[\theta]Sin[\phi] \tag{40}$$

$$y = s\,a\,Sin[\theta]Sin[\phi] \tag{41}$$

$$z = a\,Cos[\phi] \tag{42}$$

a, θ, ϕ are inverse functions given by (43)-(45).

$$a = \pm\sqrt{x^2 + \left(\frac{y}{s}\right)^2 + z^2} \tag{43}$$

$$\theta = arcTan\left[\frac{y}{s\,x}\right] \tag{44}$$

$$\phi = arcTan\left[\frac{\sqrt{x^2 + \left(\frac{y}{s}\right)^2}}{z}\right] \quad \textbf{(45)}$$

In these equations the coordinate system behaves like spherical coordinates but is skewed in the y direction by the factor s. The factor s can be determined using the least squares estimate of the form $A = sB$, where A are the positions $A = [Apex\ Inner, Apex\ Outer] = [6, 8]cm$ and B are the positions $B = [Basal\ Inner, Basal\ Outer] = [2, 3]cm$. All positions are measured from the origin which is located at the center of the base of the left ventricle (Cartesian position (0, 0, 0)). s was found as 2.71. The bounds of the coordinates were $a = [2, 3]$, $\theta = [0, \pi]$ and $\phi = [0, \pi]$. These boundaries form the shape shown in Figure 16 panel a with a reported volume of $108\ mL$.

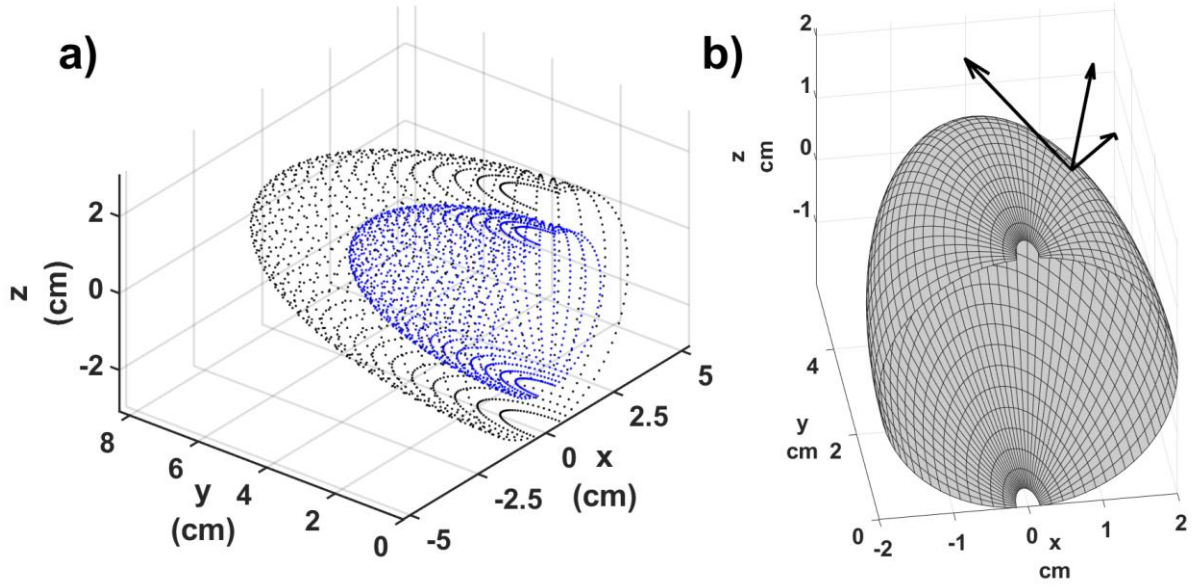

Figure 16 - a) Model of the myocardium. Model boundaries are shown in blue ($a = 2$) and black ($a = 3$), respectively. b) A surface of myocardium depicted in skewed spherical coordinates with corresponding base vectors $\hat{e}_a$, $\hat{e}_\theta$ and $\hat{e}_\phi$ at point $a = 2$, $\theta = \frac{\pi}{4}$ and $\phi = \frac{\pi}{4}$.

The bioelectrical activity of the myocardium is represented using the Bueno-Orovio-Fenton-Cherry RD model (BOFC) [22]. BOFC assumes there are three major currents, fast inward, slow inward, and slow outward. BOFC is described by (46)-(52).

$$\frac{du}{dt} = \mathrm{D}\nabla^2 u - (J_{fi} + J_{so} + J_{si}) + J_{Sim} \tag{46}$$

$$\frac{dv}{dt} = \frac{(1 - H[u - \theta_v])(v_\infty - v)}{\tau_v^-} - \frac{H[u - \theta_v]v}{\tau_v^+} \tag{47}$$

$$\frac{dw}{dt} = \frac{(1 - H[u - \theta_w])(w_\infty - w)}{\tau_w^-} - \frac{H[u - \theta_w]w}{\tau_w^+} \tag{48}$$

$$\frac{ds}{dt} = \frac{\left(\frac{(1 + tanh[k_s(u - u_s)])}{2} - s\right)}{\tau_s} \tag{49}$$

$$\mathrm{J_{fi}} = \frac{-\mathrm{v\,H[u - \theta_v](u - \theta_v)(u_u - u)}}{\tau_{\mathrm{fi}}} \tag{50}$$

$$\mathrm{J_{so}} = \frac{(\mathrm{u - u_o})(1 - \mathrm{H[u - \theta_w]})}{\tau_{\mathrm{o}}} + \frac{\mathrm{H[u - \theta_w]}}{\tau_{\mathrm{so}}} \tag{51}$$

$$\mathrm{J_{si}} = \frac{-\mathrm{H[u - \theta_w]ws}}{\tau_{\mathrm{si}}} \tag{52}$$

The four variables are $u, v, w\ and\ s$. u represents the transmembrane potential and v, w, and s are gating variables that model the protein gating dynamics of myocardial cells. The function H is the Heaviside or step function. D is the diffusion coefficient and was considered homogeneous throughout the myocardium. In our study, D was set to 4.7 $\frac{cm^2}{sec}$. This value of D is higher than the diffusivity proposed by Bueno-Orovio et al. (1.2 $\frac{cm^2}{sec}$) [22] to allow wave propagation through the areas of myocardium with higher curvature imposed by the skewed

spherical coordinates. J_{Stim} represents the Purkinje fibers which provide a stimulus current that raises the transmembrane potential above a threshold to initiate an AP. J_{Stim} traveled in the θ direction with a constant speed of 3 $\frac{m}{sec}$ and stimulated the volume enclosed by $a = [2.05, 2.15]\ cm$ and $\phi = [.5, 2.5]\ rads$ and $\theta \pm \frac{\pi}{40}\ rads$ starting at $\theta = 0\ rads$ and ending at $\theta = 3\ rads$. These boundaries approximate the location and activation sequence of the Purkinje fibers within the LV [47]. The parameters used are described in Table 1. Remaining BOFC equations are shown in Appendix A.

Laplacian operator for the coordinates (43)-(45) is shown by (53).

$$\nabla^2 u = g^{aa}\frac{\partial^2 u}{\partial a^2} + g^{\theta\theta}\frac{\partial^2 u}{\partial \theta^2} + g^{\phi\phi}\frac{\partial^2 u}{\partial \phi^2} + 2g^{a\theta}\frac{\partial^2 u}{\partial a \partial \theta} + 2g^{a\phi}\frac{\partial^2 u}{\partial a \partial \phi} + 2g^{\theta\phi}\frac{\partial^2 u}{\partial \theta \partial \phi} + \left(g^{\theta\theta}\, a + g^{\phi\phi} a\, Sin[\phi]^2\right)\frac{\partial u}{\partial a} - 2\left(\frac{g^{a\phi}}{a} + g^{\theta\phi} Cot[\phi]\right)\frac{\partial u}{\partial \theta} + \left(\frac{g^{\phi\phi} Sin[2\phi]}{2} - \frac{2\, g^{a\theta}}{a}\right)\frac{\partial u}{\partial \phi} \quad \textbf{(53)}$$

(53) contains elements from the inverse metric tensor (g^{ij}) and Christoffel coefficients (Γ_{ij}^{k}) which are reported in Appendix A. No-flux boundary conditions reflect the absence of diffusive fluxes at the boundaries of the myocardium and are defined by (54).

$$\nabla u \cdot \hat{n} = 0 \qquad on\ \partial\Omega \quad \textbf{(54)}$$

Cell Types

Model parameters were defined to approximate the cellular characteristics of different cell types within the myocardium. Three different cell types were considered for the model which include Epicardial, Endocardial and Mid-Myocardial cells. All parameters were originally set for mid-myocardial cells [22] and subsequently modified for epicardial and endocardial cells to reflect shorter and longer APD, respectively (Figure 17). By varying 2 parameters, τ_{so_1} and k_s, three different AP were considered for each cell type. The APD gradient increased from Epicardial to Endocardial area of myocardium in a linear fashion as previously shown [48,49]. The parameters used are listed in Table 1.

Using the parameters in Table 1, the APs vary as shown in Figure 17.

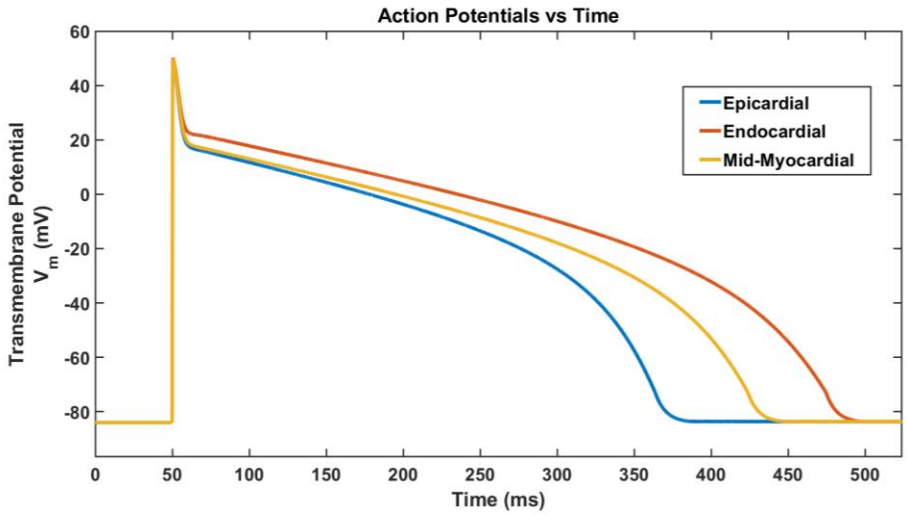

Figure 17 - Action potentials computed in different areas of myocardium. The AP curves represent the linear growth of APD from the shortest value of 325ms in the Epicardial area to its longest value of 450ms in the Endocardial area.

Table 1. Parameters for epicardial, endocardial and mid-myocardial cells which are used in the BOFC equations (46)-(52). All parameters are equal except τ_{so_1} and k_s.

	Epicardial	Endo-cardial	Mid-Myo-cardial		Epicardial	Endo-cardial	Mid-Myo-cardial
u_o	0.000	0.000	0.000	τ_{fi}	0.078	0.078	0.078
u_u	1.610	1.610	1.610	τ_{o_1}	410.000	410.000	410.000
θ_v	0.300	0.300	0.300	τ_{o_2}	7.000	7.000	7.000
θ_w	0.130	0.130	0.130	τ_{so_1}	41.250	52.500	45.000
θ_v^-	0.100	0.100	0.100	τ_{so_2}	0.800	0.800	0.800
θ_o	0.005	0.005	0.005	k_{so}	2.100	2.100	2.100
$\tau_{v_1}^-$	80.000	80.000	80.000	u_{so}	0.600	0.600	0.600
$\tau_{v_2}^-$	1.451	1.451	1.451	τ_{s_1}	2.734	2.734	2.734
τ_v^+	1.451	1.451	1.451	τ_{s_2}	4.000	4.000	4.000
$\tau_{w_1}^-$	70.000	70.000	70.000	k_s	1.500	1.250	1.250
$\tau_{w_2}^-$	8.000	8.000	8.000	u_s	0.9087	0.9087	0.9087
k_w^-	200.000	200.000	200.000	τ_{si}	3.385	3.385	3.385
u_w^-	0.016	0.016	0.016	$\tau_{w\infty}$	0.010	0.010	0.010
τ_w^+	280.000	280.000	280.000	w_∞^*	0.500	0.500	0.500

The APD for the Epicardial is the shortest and the APD for Endocardial is the longest. The difference between the Endocardial and Epicardial was calculated to be approximately 100ms apart. The thicknesses of the Endocardium and Epicardium were considered 20% of the thickness of the entire myocardium with the mid-myocardium covering the remaining 60% between the Epicardium and Endocardium. Thickness is associated with the coordinate a in the skewed spherical coordinates. All three cell types were considered to cover the span of the 3D model where span consists of the coordinates $\theta$and ϕ and from bounds 0 to π for both.

Numerical Solutions

To solve (46)-(52) we implemented first and second order finite difference approximation with respect to temporal, Δt, and spatial, Δx, grid steps, respectively ((55)-(57)).

$$\frac{\partial^2 u}{\partial x^2} = \frac{u(x+\Delta x) - 2u(x) + u(x-\Delta x)}{\Delta x^2} + \mathcal{O}(\Delta x^2) \quad \textbf{(55)}$$

$$\frac{\partial u}{\partial x} = \frac{u(x+\Delta x) - u(x-\Delta x)}{2\Delta x} + \mathcal{O}(\Delta x^2) \quad \textbf{(56)}$$

$$\frac{\partial u}{\partial t} = \frac{u(t+\Delta t) - u(t)}{\Delta t} + \mathcal{O}(\Delta t) \quad \textbf{(57)}$$

Denoting a temporal node using a superscript t and spatial nodes a, θ, and ϕ using subscripts ijk, one can derive a discretized set of (46)-(52) as (58)-(64).

$$u_{ijk}^{t+1} = u_{ijk}^{t} + \Delta t\left(D\widehat{\nabla}^2 u_{ijk}^{t} - \left(J_{fi} + J_{so} + J_{si}\right) + J_{Stim}\right) \quad \textbf{(58)}$$

$$v_{ijk}^{t+1} = v_{ijk}^{t} + \Delta t\left(\frac{(1 - H[u_{ijk}^{t} - \theta_v])(v_\infty - v_{ijk}^{t})}{\tau_v^-} - \frac{H\left[u_{ijk}^{t} - \theta_v\right]v_{ijk}^{t}}{\tau_v^+}\right) \quad \textbf{(59)}$$

$$w_{ijk}^{t+1} = w_{ijk}^{t} + \Delta t\left(\frac{(1 - H[u_{ijk}^{t} - \theta_w])(w_\infty - w_{ijk}^{t})}{\tau_w^-} - \frac{H\left[u_{ijk}^{t} - \theta_w\right]w_{ijk}^{t}}{\tau_w^+}\right) \quad \textbf{(60)}$$

$$s_{ijk}^{t+1} = s_{ijk}^{t} + \Delta t\left(\frac{\left(\frac{(1 + tanh[k_s(u_{ijk}^{t} - u_s)])}{2} - s_{ijk}^{t}\right)}{\tau_s}\right) \quad \textbf{(61)}$$

$$\mathrm{J_{fi}} = \frac{-v_{ijk}^{t}\,\mathrm{H}\left[u_{ijk}^{t} - \theta_\mathrm{v}\right]\left(u_{ijk}^{t} - \theta_\mathrm{v}\right)(\mathrm{u_u} - u_{ijk}^{t})}{\tau_\mathrm{fi}} \quad \textbf{(62)}$$

$$\mathrm{J_{si}} = \frac{-\mathrm{H}\left[u_{ijk}^{t} - \theta_\mathrm{w}\right]w_{ijk}^{t}s_{ijk}^{t}}{\tau_\mathrm{si}} \quad \textbf{(63)}$$

$$\mathrm{J_{so}} = \frac{(u_{ijk}^{t} - \mathrm{u_o})(1 - \mathrm{H}\left[u_{ijk}^{t} - \theta_\mathrm{w}\right])}{\tau_\mathrm{o}} + \frac{\mathrm{H}[u_{ijk}^{t} - \theta_\mathrm{w}]}{\tau_\mathrm{so}} \quad \textbf{(64)}$$

$\widehat{\nabla}^2 u_{ijk}^{t}$ represents the discretized Laplacian (58) which is presented in Appendix A. The spatial discretization values are $\Delta a = .025\ cm$, $\Delta\theta = .025\pi\ rads$ and $\Delta\phi = .025\pi\ rads$ and the temporal discretization step is $\Delta t = .02\ ms$. The no-flux boundary conditions incorporated an imaginary node which was extended beyond the boundaries to keep the second order of numerical approximation of the boundary conditions.

***In silico* ECG**

Calculating the ECGs was performed assuming that the human torso is a homogeneous infinite conductor[31,32]. The myocardium was considered as an aggregate of multiple dipoles which induced surface quasistatic electric field with a potential described by (65).

$$\Phi = \frac{1}{4\pi\sigma}\int_\tau \vec{J}^{i} \cdot \nabla\left(\frac{1}{r}\right)d\tau \quad \textbf{(65)}$$

τ is volume, J^i is the source current which is defined as $D\nabla u$, r is the position from the source current to the recording electrode and σ is the conductivity of the homogenous torso. (65) was solved numerically using trapezoidal method.

Recording Electrode Placement

Using (65), a potential difference or lead voltage between two recording electrodes was computed for 4 electrodes located outwards from the apex of the left ventricle as shown in Figure 18 and Table 2.

Table 2. Electrode positions E1, E2, E3 and E4 calculated in cartesian coordinates and measured relative to the origin located at the center of the base of the left ventricle model. All positions measured in centimeters. The area enclosed between the electrodes is equal to 100 cm^2.

Electrode # - (x, y, z) cm	
E1 – (5, 15, -5)	E2 – (-5, 15, -5)
E3 – (5, 15 ,5)	E4 – (-5, 15, 5)

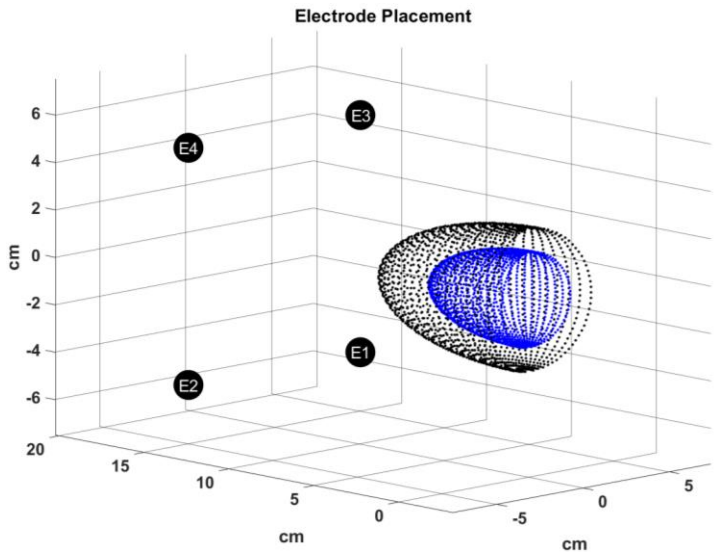

Figure 18 - The positions of four electrodes with respect to the location of the left ventricle model.

Four lead voltages (ECG signals) were computed as shown in Table 3.

Table 3. Description of leads L1, L2, L3 and L4. Each lead is composed of two of the four electrodes E1, E2, E3 and E4.

Leads	
L1 = E4 – E3	L2 = E4 – E1
L3 = E4 – E2	L4 = E2 – E1

Stochastic *in silico* ischemia and QT Interval

We implement stochastic parameters to generate data suitable for training a 1D CNN. These parameters control the severity and configuration of ischemic zones and ischemic APD. We define severity of ischemia as the magnitude of changes of parameter u_o inside an ischemic zone (Table 1). The difference between the increased value of resting potential, u_o', and its initial value u_o is defined as a severity of ischemia and is denoted as a $\gamma = \mathrm{u}_o' - u_o$. Figure 19 demonstrates that the action potential upstroke practically does not depend on γ. However, only 10% increase in γ yields to two-fold decrease in APD which signifies the growth of the myocardial ischemic zone.

Values of parameter γ are stochastically produced using a continuous uniform random number generator (CURNG) within the range between 0 and 0.2. Examples of action potentials for cells with different severity of ischemia are shown in Figure 19.

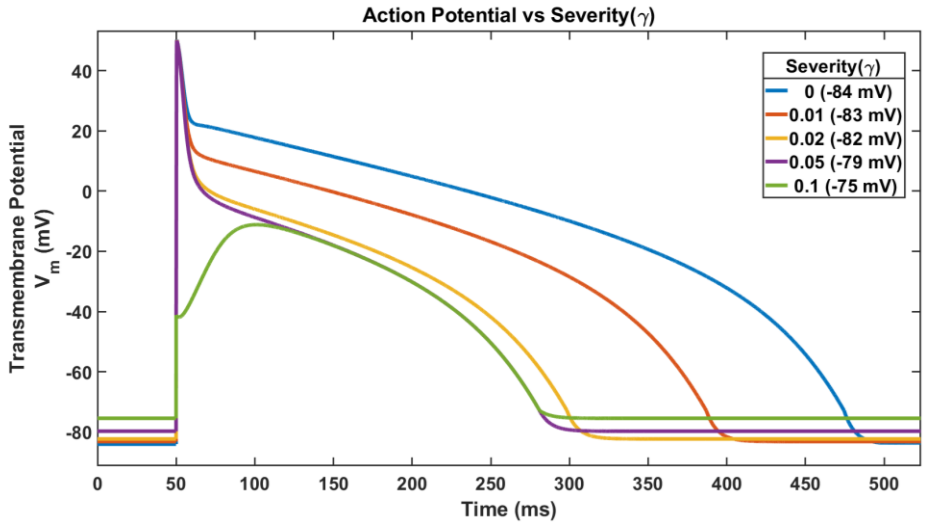

Figure 19 - Dependence of action potential on parameter γ in Endocardium.

Configuration and volumes of ischemic zones which include conglomerates of ischemic cells are determined by (66).

$$Volume = \int_{a_1}^{a_2} \int_{\theta_1}^{\theta_2} \int_{\phi_1}^{\phi_2} s\, a^2 Sin[\phi]\, da\ d\theta\, d\phi \tag{66}$$

Integral limits are determined stochastically. $sa^2Sin[\phi]$ is the volume element calculated from the determinate of the metric tensor for skewed spherical coordinates that is described in Appendix A. The limits are determined by measuring six arc lengths with respect to coordinates of the point *P* located within the boundaries of the left ventricle model (Figure 16 Panel a). These stochastic coordinates are determined by applying a CURNG. Using point *P* as an origin, the CURNG determines an arc length within the range of 0 to .5 which corresponds to half of the length of the ventricle model boundaries between $a = 2$ and $a = 3$. This length is added and

subtracted to the a coordinate of the point *P* and produces the limits a_1 and a_2, respectively. The limits a_1 and a_2 are used to calculate an arc length s_a (67). The arc lengths s_θ and s_ϕ are also determined using a CURNG which in this case is implemented in the range between s_a and $2\ s_a$. Like for limits a_1 and a_2, half of the lengths of s_θ and s_ϕ are added and subtracted from the coordinates of stochastic point *P* to determine the limits θ_1, θ_2, ϕ_1 and ϕ_2. Finally, all arc lengths can be obtained by (67)-(69).

$$s_a = \int_{a_1}^{a_2} \sqrt{g_{aa}}\, da \tag{67}$$

$$s_\theta = \int_{\theta_1}^{\theta_2} \sqrt{g_{\theta\theta}}\, d\theta \tag{68}$$

$$s_\phi = \int_{\phi_1}^{\phi_2} \sqrt{g_{\phi\phi}}\, d\phi \tag{69}$$

g_{aa}, $g_{\theta\theta}$ and $g_{\phi\phi}$ denote components of the metric tensor for the skewed spherical coordinates. Example of arc lengths are depicted in Figure 20. The limits a_1, a_2, θ_1, θ_2, ϕ_1 and ϕ_2 in the integrals in (67)-(69) define the boundaries of the ischemic zone. Factor γ and the boundaries of the ischemic zone will be referred to as ischemic zone parameters.

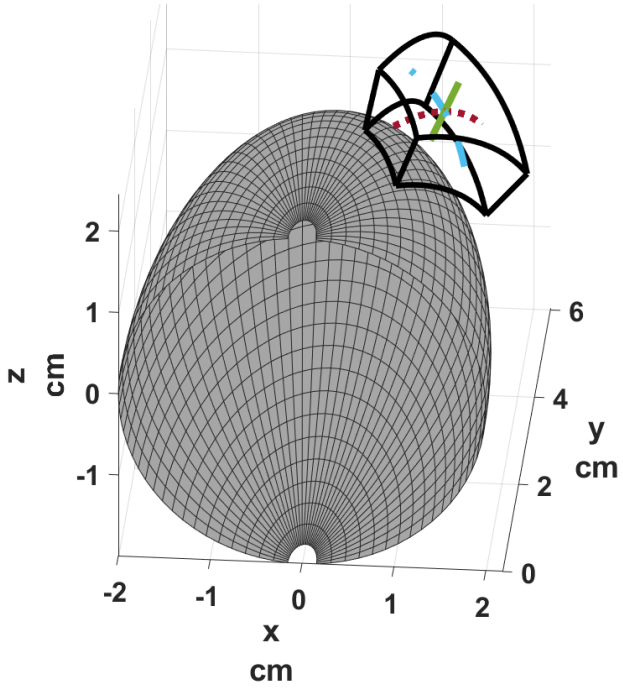

Figure 20 - Arc lengths s_a, s_θ and s_ϕ are shown in green, blue, and maroon, respectively. Ischemic zone is defined within the volume enclosed by the black curves. Intersection of the three arcs denote is denoted as point P. Grey surface reflects the endocardial surface at $a = 2$.

Stochastic APDs (QT interval) variations are controlled by varying τ_{so_1} from $0.6\tau_{so_1}$ to τ_{so_1} in all cell types inside and outside the ischemic zone using CURNG (Table 1, Figure 20). This allowed the QT interval to fluctuate between 250ms and 400ms.

Solving (58)-(65) we compute ECG signals which demonstrate the effects of an ischemic zone placed at the apex of the model with a QT interval of 400ms (Figure 21)

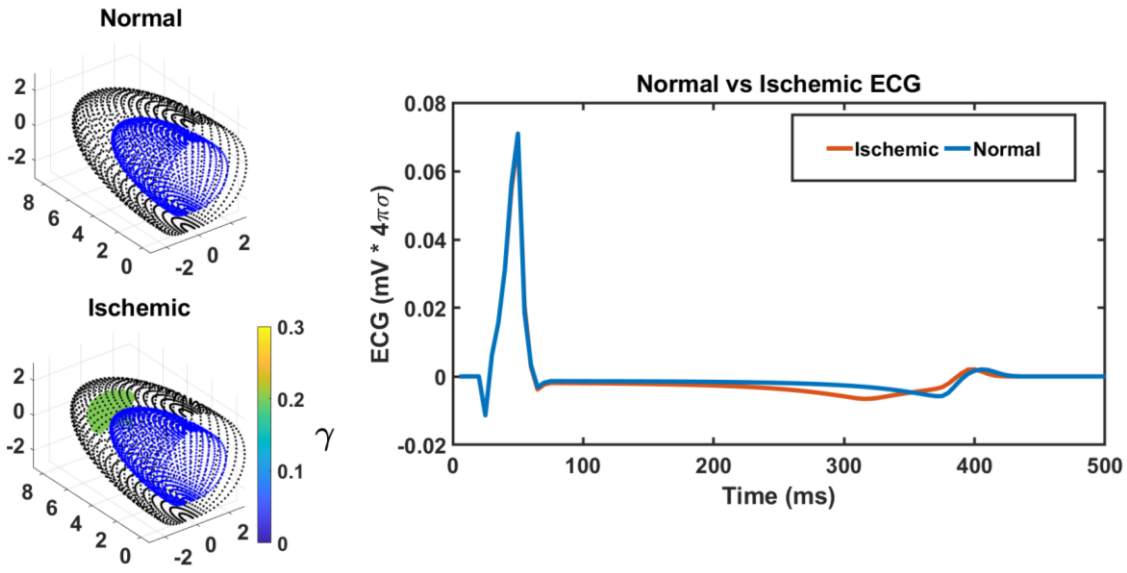

Figure 21 - Normal vs Ischemic ECG computed in lead L1 (see Table 3 and (46)-(52)). Ischemic mass (green) is in the apex of the myocardium. Parameters of ischemic zone are as follows: $\gamma = .2$, $a_1 = 2.25$, $a_2 = 2.75$, $\theta_1 = .4\pi$, $\theta_2 = .6\pi$, $\phi_1 = .4\pi$ and $\phi_2 = .6\pi$.

1D CNN

Using the methods described above, we computed 20,000 *in silico* ECGs like those depicted in Figure 21 with stochastic ischemic zones parameters. The values of the stochastic *in silico* ischemic zone parameters and corresponding ECG signals were stored in a database for training a 1D CNN.

Inputs of a 1D CNN are composed of a single beat *in silico* RD signal projected to one or more corresponding ECG lead (Table 3). The inputs are used to predict the outputs correlated with the 7 *in silico* ischemic zone parameters. Inputs are initially processed using four 1D convolutional layers (Figure 22, Part A). Part A is connected to a dense neural network via a dropout, flatten and pooling layers (Figure 22, Part B). Part B is connected to four dense layers and an output layer of size seven (Figure 22, Part C). The size of the output layer correlates with the stochastic *in silico* ischemic zone parameters described above. The input signals are scaled to

the max voltage of lead 1 (L1) and the *in silico* ischemic zone parameters are normalized using respective model boundaries of $a = [2, 3]$, $\theta = [0, \pi]$ and $\phi = [0, \pi]$

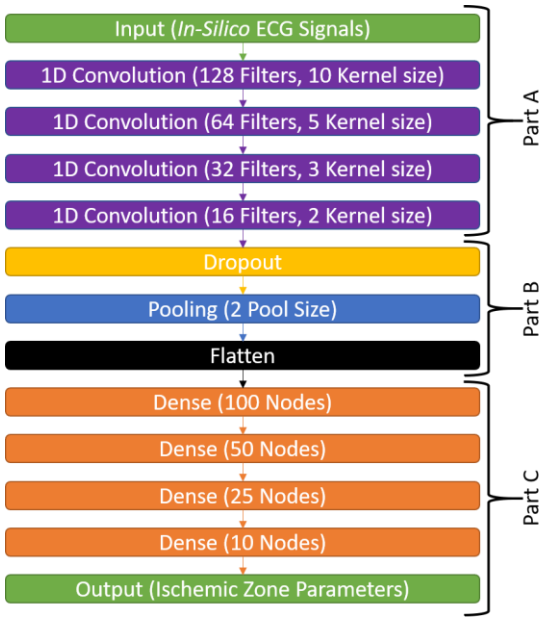

Figure 22 - Framework of the 1D CNN. Part A represents the Convolutional cluster. Part B is the processing cluster to connect part A to part C. Part C is the cluster of dense neural layers relating the convolutions to the *in silico* ischemic zone parameters.

The first layer in Figure 22 convolutes the input layer using 132 different filters with kernel sizes of 10. The convolution between these filters is passed to the next layer of 64 filters with kernel of size 5. This process continues through two more convolutional layers of 32 and 16 filters and of kernel size 3 and 2, respectively. All the convolutional layers used rectified linear unit (ReLU) activation functions. To allow slower and better training, a dropout layer was included with a drop out value of 0.5. This correlates with half of the previous layer's nodes being randomly selected to update the next layer. The following layer is a max pooling layer which reduces data by selecting the max value in set pool sizes to prevent overfitting. The pool

size was set to 2. The data was flattened to an array to connect the dense network to the convolutional network. The dense network is a serial connection of four dense neural layers. They decreased in size from 100, 50, 25 to 10 nodes, respectively. All dense layers use the ReLU activation function. The output layer has 7 nodes correlating with the prediction of the *in silico* ischemic zone parameters. The implementation of a described above 1D CNN is completed using Python IDE [50] with Keras deep learning package [51].

The *in silico* ECG database has been split for training, validating, and testing the performance of the 1D CNN in prediction of the *in silico* ischemic zone parameters. In particular, the 80:20 ratio is used for training and testing sets while a validation set is taken from the training set in the same 80:20 proportion. An instance refers to an occurrence of an *in silico* ischemic zone parameters within any of these sets. Mean absolute error (MAE) is determined with respect to the *in silico* ischemic zones parameters of the validation set and the predicted ischemic zone parameters of the 1D CNN. Training of the 1D CNN continues until the MAE stops decreasing. MAE, squared error (SE_i) and mean squared error (MSE) are metrics used to validate the 1D CNN and are defined by (70)-(72).

$$MAE = \frac{1}{n}\sum_{i}^{n}\sum_{j}^{m} Abs[y_{ij} - f_{ij}] \tag{70}$$

$$SE_i = \sum_{j}^{m}(y_{ij} - f_{ij})^2 \tag{71}$$

$$MSE = \frac{1}{n}\sum_{i}^{n} SE_i \tag{72}$$

y_{ij} are the *in silico* ischemic zone parameters and f_{ij} are the 1D CNN predicted ischemic zone parameters. i is the index for instance and j is the index for the ischemic zone parameters. Values of n are equal to the number of instances in the set and m is equal to 7.

Once training is completed, the efficacy of 1D CNN predictions is assessed using the coefficient of determination (COD) or r^2. r^2 is used to quantify the effect of number of leads utilized in training of the 1D CNN. It is defined by (73)-(76).

$$\overline{y_j} = \frac{1}{n}\sum_{i=1}^{n} y_{ij} \tag{73}$$

$$S_j^0 = \sum_{i=1}^{n}\left(y_{ij} - \overline{y_j}\right)^2 \tag{74}$$

$$S_j = \sum_{i=1}^{n}\left(y_{ij} - f_{ij}\right)^2 \tag{75}$$

$$r_j^2 = 1 - \frac{S_j}{S_j^0} \tag{76}$$

i, j, n and m are the same as (70)-(72). r_j^2 is determined for each ischemic zone parameter, j, individually. The indices of j, from 1 to 7, represent the *in silico* ischemic zone parameters in the order γ, a_1, a_2, θ_1, θ_2, ϕ_1 and ϕ_2, respectively.

Results and Discussion

r^2 and number of leads

Using the database of *in silico* ECGs and the associated stochastic ischemic zone parameters, described above, we trained the 1D CNN using cases with varying number of input ECG leads. The r_j^2 values for different cases are shown in Table 4.

Table 4. List of the r_j^2 and $r^2\ average$ values for the ischemic zone parameters predicted by trained CNNs.

Case #	# Of Leads	$r_1^2\ (\gamma)$	$r_2^2\ (a_1)$	$r_3^2\ (a_2)$	$r_4^2\ (\theta_1)$	$r_5^2\ (\theta_2)$	$r_6^2\ (\phi_1)$	$r_7^2\ (\phi_2)$	$r^2 Average$
1	1	0.54	0.75	0.79	0.77	0.77	0.79	0.78	0.74
2	1	0.58	0.75	0.79	0.77	0.78	0.85	0.84	0.77
3	2	0.62	0.82	0.86	0.87	0.87	0.91	0.90	0.84
4	2	0.71	0.82	0.91	0.92	0.90	0.95	0.95	0.88
5	2	0.69	0.83	0.88	0.85	0.86	0.92	0.92	0.85
6	3	0.73	0.85	0.88	0.89	0.90	0.91	0.91	0.87
7	3	0.70	0.83	0.87	0.84	0.83	0.93	0.93	0.85
8	4	0.70	0.83	0.88	0.82	0.83	0.92	0.92	0.84
9	4	0.72	0.86	0.90	0.89	0.90	0.93	0.93	0.87

Figure 23 explains the effect of number of leads on efficacy of training the 1D CNN. It shows that $r^2\ average$ practically saturates for numbers of leads ranging between two and four increasing only by 3.5%. It's worth to notice that the $r_2^2\ (a_1)$ is lower in than the $r_3^2\ (a_2)$ which indicates that our approach determines *in silico* ischemic zone edges near the epicardial surface ($a = 3$) better than near the endocardial surface ($a = 2$). As the number of leads increases, the theoretical maximum of $r^2\ average$ can be evaluated as a horizontal asymptote of the function $a + \frac{b}{x^2}$ shown in Figure 24.

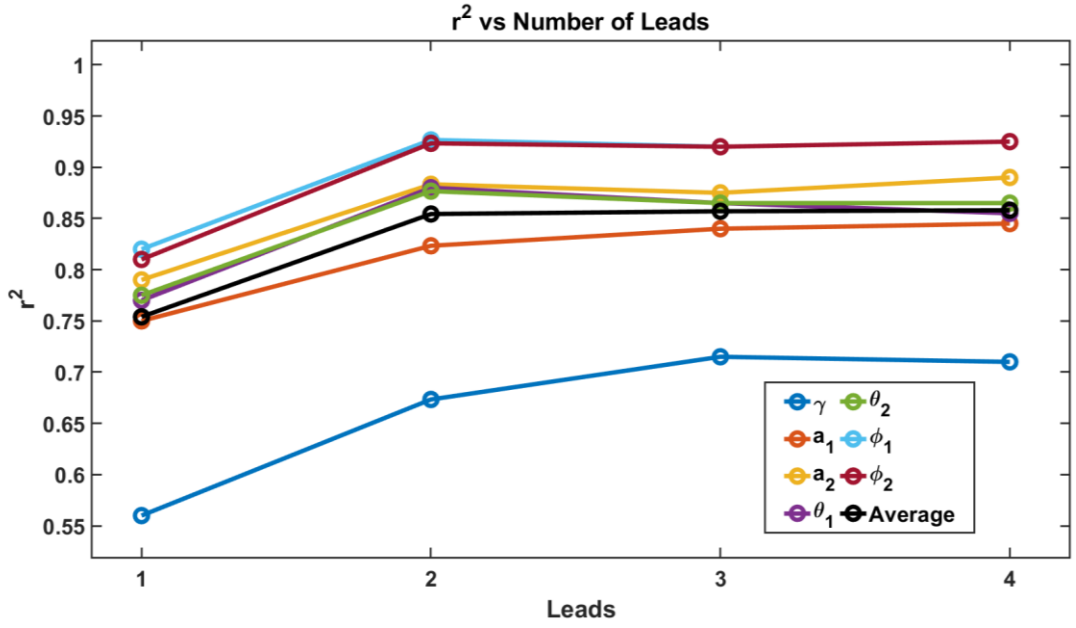

Figure 23 - Dependence of r_j^2 and r^2 $average$ on the number of leads. Table 4 columns are averaged over cases with the same number of leads.

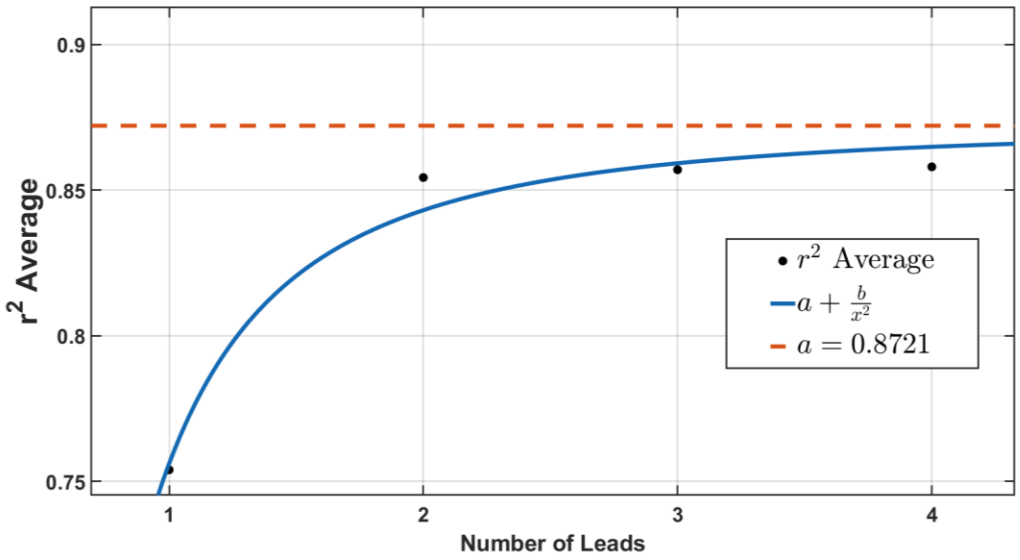

Figure 24 – Dependence of theoretical r^2 $average$ on number of leads (x). Blue curve is determined by fitting the function $f(x) = a + \frac{b}{x^2}$. The value of a is equal to 0.8721.

Analysis of 2-lead trained 1D CNN

Figure 25 shows an example of stochastic *in silico* ischemic zones parameters and predicted ischemic zones parameters generated by a 2-lead trained 1D CNN (Table 4, case 4) with MSE of 0.2404.

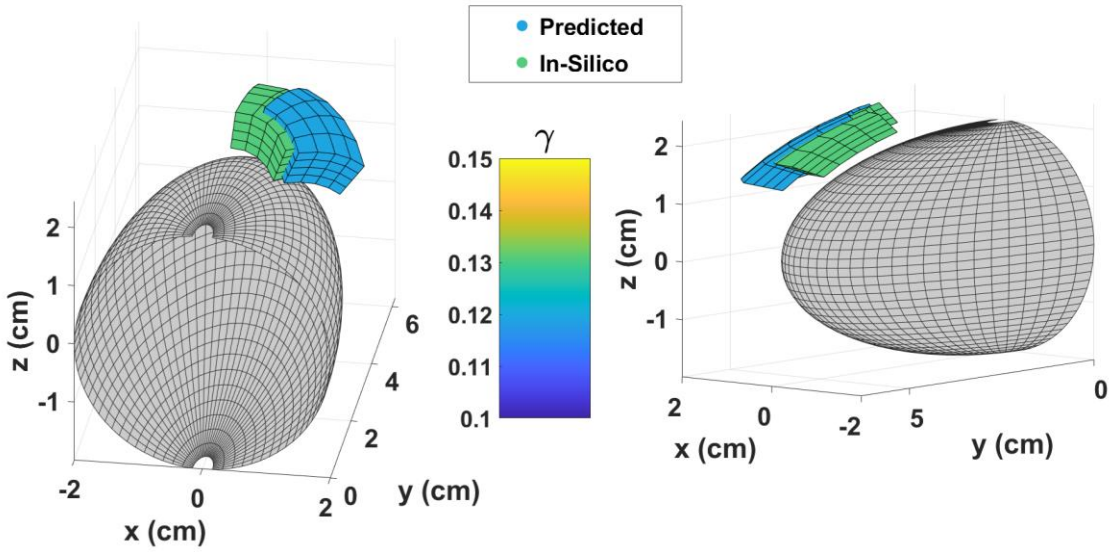

Figure 25 - Two different views of the *in silico* and predicted ischemic zones shown in blue and green, respectively. Predicted and *in silico* values of γ are equal to 0.1191 and 0.1307, respectively. Grey surface reflects the Endocardial surface at $\alpha = 2$.

A validation of such training is attained by comparing the SE_i to the MSE. Figure 26 shows that most of the instances (82.35%) in the test set have SE_i below the MSE.

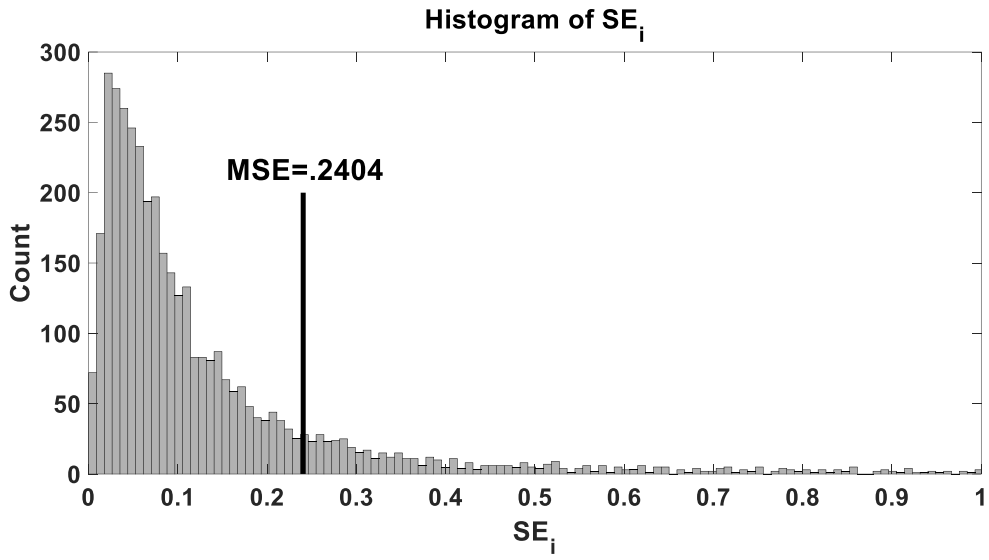

Figure 26 - Histogram of SE_i for all instances in the test set for case 4.

It should be noted that when the *in silico* ischemic zone is characterized by a lower γ value, the predicted ischemic zone has a higher value of SE_i. In particular, the average values of γ for instances with SE_i higher and lower than MSE are 0.070 and 0.106, respectively. In turn, the average volumes (see (66)) for instances with SE_i higher and lower than MSE are equal to 2.57 cm^3 and 2.39 cm^3, respectively.

Figure 27 shows how MSE varies in response to changes in values of γ and volume of the *in silico* ischemic zone. One can see those instances with very low γ have the greater MSE ranging between 1 and 3. Instances with very small ischemic volumes also have higher MSE. On the contrary, for γ greater than 0.01 and for volumes greater than 2 cm^3 the MSE decreases on the order of magnitude, proving that the 2-lead trained CNN is more effective in predicting ischemia for greater values of γ and ischemic zone volume parameters.

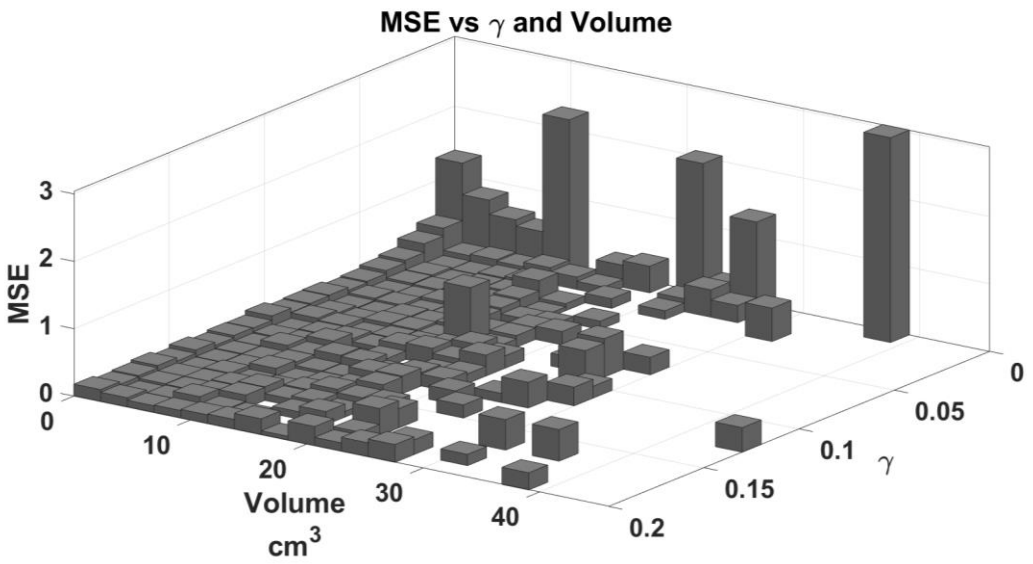

Figure 27 - Dependence of MSE on values of γ and volume of the *in silico* ischemic zone.

Conclusions

Overall, we have demonstrated the feasibility of using a 1D CNN to detect the configuration and severity of myocardial ischemia based on ECG measurements using just a few surface leads. Unlike previous studies, we include severity of ischemia in our CNN to predict ischemia during early stages of IHD. We found that the major improvement of $r^2\ average$ by 12.58% occurs when the number of leads increases from one to two. Further increase of the number of leads does not results in feasible improvement of accuracy of ischemia detection. Based on these observations, we conclude that a two-lead configuration is sufficient to determine the ischemic zone parameters within an *in silico* left ventricle if the severity and volume are greater than 0.01 and $2\ cm^3$, respectively. This may pave the road for broader use of miniature wearable ECG devices applied in outpatient settings.

It should be noted that our numerical simulations most accurately predict ischemia in the left ventricle, so if the ischemia occurrs outside that area, the neural network described above

will most likely locate ischemia within the model bounds closest to the actual ischemia site. Similarly, the size of our model's left ventricle is exaggerated near the apex. Nonetheless, our 3D model allows for useful ischemia prediction since the maximum rRMSe has been shown to be minimal in a thick walled heart model compared to a normal wall model [52].

In our simulations, ischemia was approximated by a single variable γ which allowed us to adequately quantify major ischemic effects, but caused an overestimation of the ionic effects within the ischemic volume [21]. Likewise, non-homogenous volume conductors are known to affect the ECG amplitude [53] but were not explored in this research.

Finally, this approach to detect ischemia is based on the analysis of a single heartbeat. However, training of the neural network can be significantly more effective if implemented using a set of successive heartbeats. An inclusion of real ECG signals can increase the merit of the model by incorporating natural variability within the ECG signal. We plan to include discussed features in our future studies.

CHAPTER IV: PREDICTING FUTURE STATES OF ISCHEMIA VIA NEURAL NETWORKS: AN *IN SILICO* STUDY

Introduction

Ischemic heart disease (IHD) is one of the largest threats to public health. Every year over 9 million people die from IHD[26]. These deaths could be preventable with constant monitoring of the heart and invasive action. Currently, feasibility of constant monitoring is limited by cost, practicality, and current technology. Introduction of a process to monitor IHD and preemptively predict the changes in IHD could prove to reduce deaths worldwide significantly.

IHD typically occurs when coronary arteries around the heart become occluded and reduce the blood flow to the myocardium. When the input flow of oxygenated blood is less than the demand for oxygenated blood by the myocardium, the myocardial cells begin to die and exhibit electrophysiological changes[54]. When the coronary artery becomes completely occluded, or occluded for an extended period, the myocardial cells quickly die and may result in a myocardial infarction (MI) or heart attack. The location of the ischemic zone within the heart depends on where the occlusion of the coronary artery occurs. As the occlusion of the coronary arteries continue, the ischemic zone continues to expand, and the electrophysiological changes become more severe until the cells become completely necrotic[55,56] and become scar tissue.

The configuration of an ischemic zone varies depending on many factors such as duration, percent of coronary artery occluded, occlusion location, etc[57,58]. The general shape of ischemic zones are complex and are typically simulated using simple geometries[59]. The change from ischemic cells, within the ischemic zone, to healthy cell outside the ischemic zone are abrupt. The abrupt changes are called border zones. Border zones are typically thin and are

reported from .8 to 8 mm in width and coincide with the gradient of ionic concentrations which control the electrophysiological dynamics of myocardial cells[60,61].

IHD is normally determined using the Electrocardiogram (ECG). The ECG is a time series signal which is calculated based upon electrodynamic principles[62,63] in which the propagation of bioelectrical waves throughout the myocardium are recorded from different observation locations. Using the potential difference between multiple recording locations, called leads, clinicians can determine changes in the ECGs to approximate the configuration and severity of IHD based upon normal statistics of heart disease. Recently artificial intelligence (AI) has been applied to ECGs via deep learning/neural networks to determine heart diseases including IHD[35,64,65]. Most work has focused on classification issues to determine if IHD has occurred or classifies discrete location of ischemic zones. Unfortunately, to the authors knowledge, there is no work which peruses predicting continuous ischemic configurations in real time using AI or deep learning.

Currently, the large amount of data to train a deep learning system to predict ischemic conditions is not available due to the complexity of observing and recording ischemic events while they are occurring. The largest study, known to the authors, had 29 subjects, and used specialized devices to record the electrical activity of the heart[57]. Therefore, the use of an *in silico* model is desired to produce the data for deep learning.

As ischemia progresses, the volume and severity of ischemic zones typically increase. Determining the growth of ischemia would intel using time series data at set intervals to determine the progression of underlining characteristics within ECG signals. Convolutional neural networks (CNN) use convolutions of filters with images or signals to extrapolate data. Long-Short Term Memory[66] (LSTM) neural networks are a type of recurrent neural network

(RNN) which incorporate memory gates which allow for back propagation to occur without the vanishing gradient problem. The vanishing gradient problem occurs in an RNN when the gradient of the loss function is operated upon too many times by previous layers and the effect of backpropagation fails to update the weight of layer too far from the output layer. An LSTM, as a type of RNN, allows a neural network to use temporal data in which the previous time step affects the output of the next time step in temporally discrete data.

We propose using a simplified model for *in silico* stochastic growth of ischemic zones to train a deep learning neural network to predict the future states of ischemia. Effectiveness of the neural network will be determined via regression analysis. Analysis of the neural networks will include merit based on the number of leads applied to train the neural network. Performance of neural network will also be assessed using common ischemic type growth.

Methods

Modeling

Three-dimensional modeling of the electrophysiological dynamics of the left ventricle were completed using the same method proposed in our previous work[24] (Chapter III). The previous method approximated the electrical activity of the left ventricle while including dynamics for both normal and ischemic cells. Due to the simplistic nature of the model, simulating large amount of stochastic data is possible in a timely and efficient manner. Simulating ischemia was done in the same manner of raising the single variable u_o to produce severity ($\gamma = u_0' - u_0$) within a desired region to approximate the effects that ischemia has within the myocardium.

Stochastic Ischemic Growth and Severity

The directed random walk uses methods like previous work[67] in which a preferred direction is chosen but allows stochastic changes within specific bounds such that a defined direction is preferred. An ischemic zone is defined as the bounds which make up a volume ($a_1, a_2, \theta_1, \theta_2, \phi_1,$ and ϕ_2) and corresponding severity (γ) within a bounded domain. Initial ischemic zone ($IZ_{t+\Delta t}$) is computed via stochastic methods shown in Chapter III. After an initial ischemic zone is computed, a directed random walk is applied to allow for non-linear isotropic growth of the ischemic zone by scaling the arc lengths which comprise the ischemic zone ($S_a, S_\theta \; and \; S_\phi$).

A random step is applied within bounds of the directed direction. The direction is chosen to correlate with the slope of the line from start point (SP) to end point (EP). Time between SP and EP is normalized to 0 and 1, respectively. SP is randomly chosen using a continuous uniform random number generator (CURNG) such that $0 \leq SP \leq 1.1$. The bounds of SP represent the amount of scaling with respect to EP which is chosen to be 1 in all simulations and represent the parameters of $IZ_{t+\Delta t}$ previously calculated. Including the bound 1.1 allows for shrinking of the ischemic zone. The directed random walk uses the slope (m) between SP and EP to bound the random walk. The step size is bounded by the variable ε which allowed step size of the random step to deviate from the linear slope m. A value of $\varepsilon = 0$ indicates the random walk is completely linear and increasing ε allows for non-linearity scaling of the ischemic zone growth Each step changes temporally by an arbitrary amount where $\Delta t = \frac{1}{N}$ where N is the number of steps being taken. For this research, ε was picked using a CURNG such that $.25 \leq \varepsilon \leq .75$ for each simulation individually. Starting at EP ($S_n = 1$) and walking backwards, a random change in scale is computed and added to the previous scale value. The next scale value

is determined by using the current scaling value and shifting by the slope to the next time step to determine the new directed scaling value. The process is continued until all steps are taken. The process is described by (77).

$$S_{n-1} = S_n + \{Y(x): x \in [-\varepsilon\, m, \varepsilon\, m]\} - m\Delta t \tag{77}$$

S_n is the current scaling value, S_{n-1} is the previous scaling value and $\{Y(x): x \in [-\varepsilon\, m, \varepsilon\, m]\}$ is a random real number in the domain of $[-\varepsilon\, m, \varepsilon\, m]$. In each previous step S_{n-1} becomes the new S_n. Using this method, the scaling factors are determined in a fashion like Figure 28.

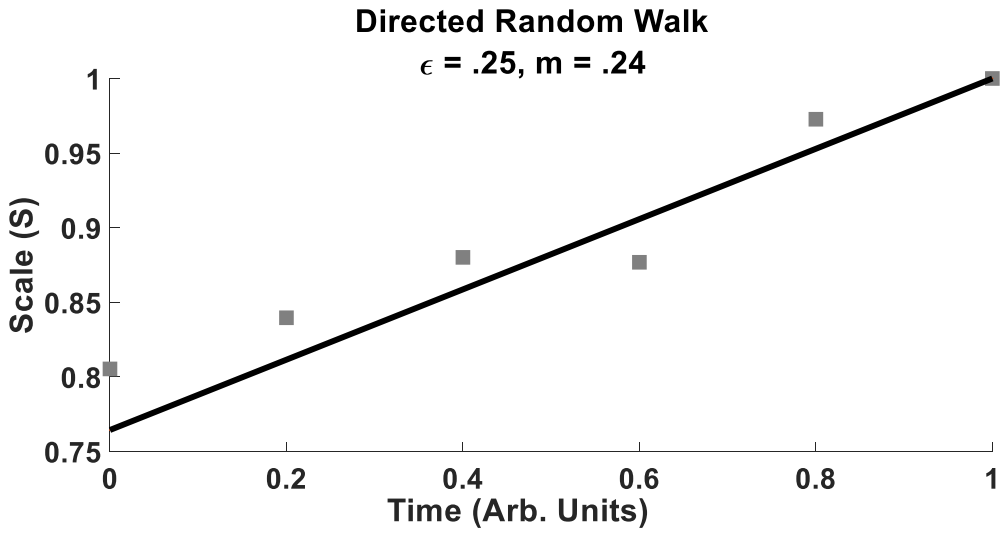

Figure 28 – Directed random walk. The scaling value will be used to create stochastic ischemic growth by varying parameters s_a, s_θ and s_ϕ.

Applying the scaling factors to the three arc lengths, mentioned earlier, in an isotropic manner, results in a growing ischemic zone volume. All ischemic zones were bounded to be within the boundaries of the model. An example of increasing size is shown in Figure 29.

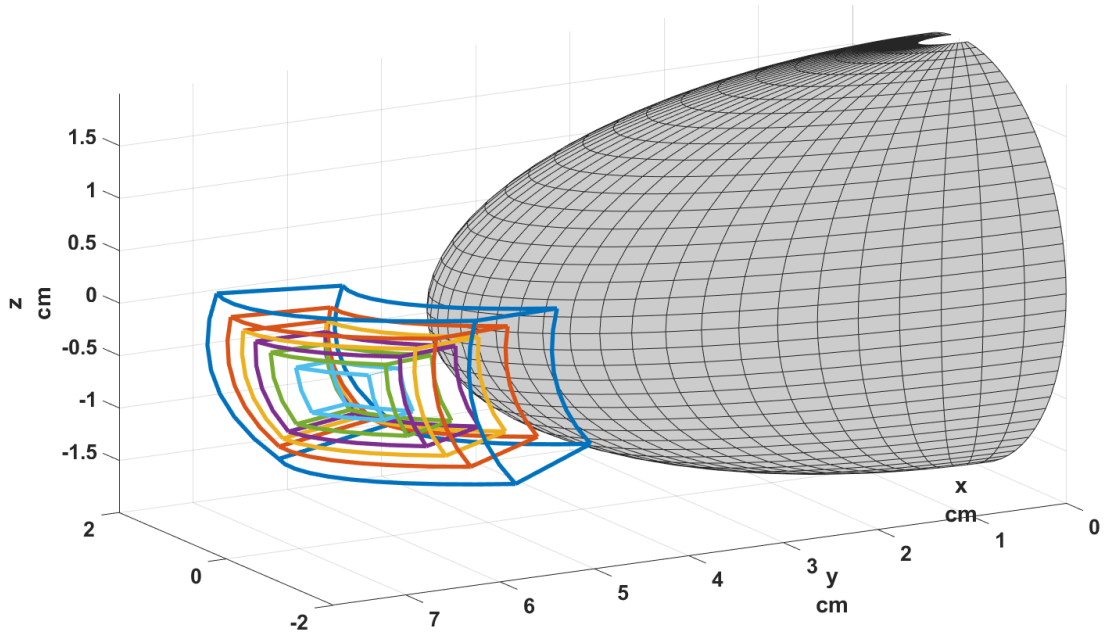

Figure 29 – Example of growing ischemic zones. The volume contained in light blue represents the IZ at $t - 4\Delta t$, the red represents the IZ at t and blue represents the IZ at $t + \Delta t$.

Using the same method, the variable γ is scaled in the same manner except the bound for SP vary depending on the slope of the random walk of the size scaling. If the slope, m, is positive, then $0 \leq SP \leq 1$ and if the slope is negative then $1 \leq SP \leq 1.1$. This method allows for more variation between the scaling of the volume and severity.

Using the stochastic directed random walk methods, the ECGs can be simulated for each temporally discrete ischemic zone. Assuming the torso as an infinite homogeneous conductor we can simulate a body surface potential by (78).

$$\Phi = \frac{1}{4\pi\sigma}\int_{\tau}\vec{J}^{i}\cdot\nabla\left(\frac{1}{r}\right)d\tau \quad \textbf{(78)}$$

Where σ is the conductivity of the torso, $\vec{J}^{i}$ is the current dipole at each point in the myocardium, r is the distance from $\vec{J}^{i}$ to the recording electrode and τ is the volume of the myocardium. Extracellular potential, Φ, is calculated at discreate time instances. Recording electrodes and leads were placed in the same positions as Chapter III. Using these methods, Figure 30 depicts the ECGs associated with lead L1 for the ischemic zones shown in Figure 30 (color coordinated).

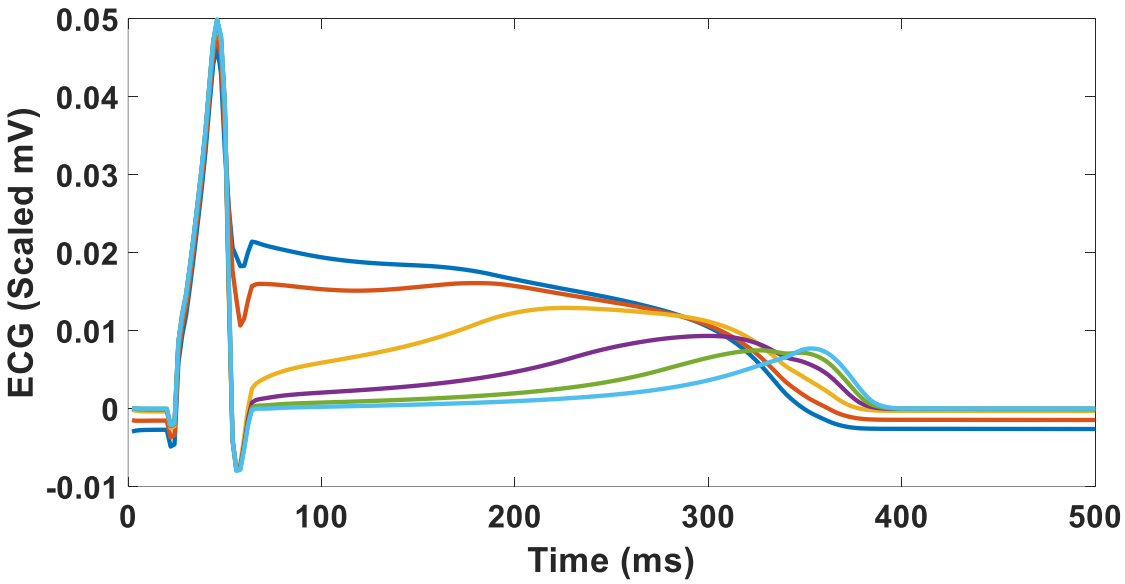

Figure 30 – ECG signals associated with the increasing size of ischemic zones in Figure 29.

1D CNN-LSTM Neural Network

To process the ECG time series data, a 1D CNN-LSTM neural network is applied to capture both the temporal and signal variations of the ischemic zones. The 1D CNN-LSTM neural network will use previous time distributed ECGs signals from multiple leads as the inputs to predict ischemic zone configuration $IZ_{t+\Delta t}$ of the next time step. Denoting the next time step with subscript $t + \Delta t$, the 1D LSTM uses $\{ECG_t, ECG_{t-\Delta t}, \dots, ECG_{t-N\Delta t}\}$ to predict IZ_t, where N is the total number of previous ECGs. In this work $N = 4$ for 5 previous time steps. Each set contained six ischemic zone parameters and the corresponding ECGs. Using Figure 29 as a reference, the dark blue ischemic zone represents $IZ_{t+\Delta t}$ and using Figure 30 for reference, all ECGs, except the dark blue, were $\{ECG_t, ECG_{t-\Delta t}, \dots, ECG_{t-N\Delta t}\}$ for that set.

Using these inputs and outputs, the layout of the 1D CNN-LSTM is displayed in Figure 31. The first layer is the input of multiple ECG leads which are time distributed for $N + 1$ previous time steps. The four 1D Convolutional layers (purple) decrease in number of filters and kernel size. The convolutional layers are connected to a dropout, pooling and flatten layers which slow training, decrease data size and flatten the data, respectively. The four dense layers (orange) decrease in number of nodes and process data from the convolutional layers to be used with the LSTM layer. The LSTM layer (gray) uses time distributed data from the dense layers in sequential order to predict the next time steps ischemic zone. The final layer is the output layer which correlates with the ischemic zone parameters $IZ_{t+\Delta t}$.

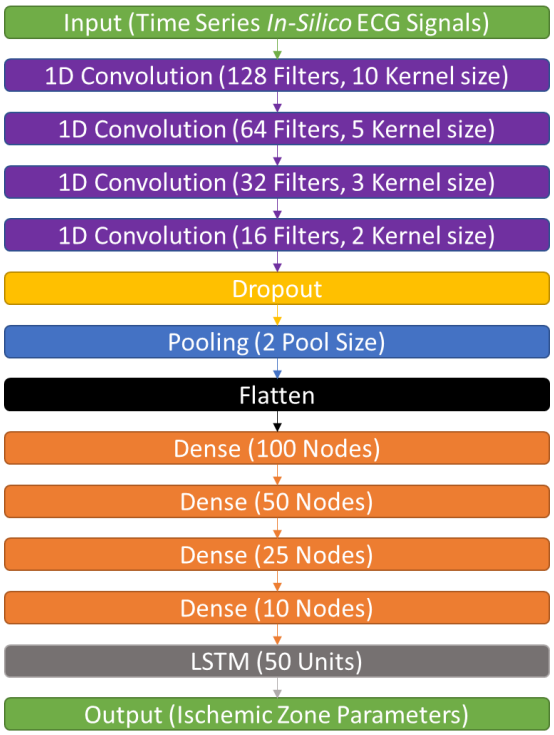

Figure 31 – Layout of the 1D CNN-LSTM. The multiple ECG lead inputs are distributed across different times and are processed by all the layers separately until the LSTM layer which process the incoming data sequentially.

Results and Discussions

Performance of 1D CNN-LSTM

Using the method presented above, over 10,000 stochastic *in silico* growing ECGs were computed. After training different neural network layouts, the layout shown in Figure 31 had the optimal performance. Using this layout, the performance with respect to number of leads used in training was recorded in Table 5.

Table 5 – Coefficient of determination (r^2) for multi-regression analysis of the 1D CNN-LSTM for all IZ parameters. Different cases show the performance of the 1D CNN-LSTM depending on the number of leads used in the training process.

Case Number	Number of Leads	r^2 $Average$	$r_1^2\ (\gamma)$	$r_1^2\ (a_1)$	$r_1^2\ (a_2)$	$r_1^2\ (\theta_1)$	$r_1^2\ (\theta_2)$	$r_1^2\ (\phi_1)$	$r_1^2\ (\phi_2)$
1	2	0.598	0.32	0.52	0.67	0.65	0.65	0.68	0.69
2	2	0.703	0.54	0.67	0.72	0.70	0.70	0.80	0.80
3	3	0.701	0.50	0.63	0.65	0.73	0.74	0.83	0.82
4	3	0.702	0.49	0.66	0.73	0.71	0.73	0.80	0.79
5	4	0.764	0.58	0.71	0.78	0.79	0.79	0.85	0.85
6	4	0.767	0.55	0.77	0.80	0.77	0.78	0.84	0.85
7	4	0.805	0.65	0.77	0.79	0.83	0.83	0.89	0.88

Averaging the cases which had the same number of leads used resulted in a general trend of mostly linear increase in r^2 as the number of leads increased. These overall trends are shown in Figure 32.

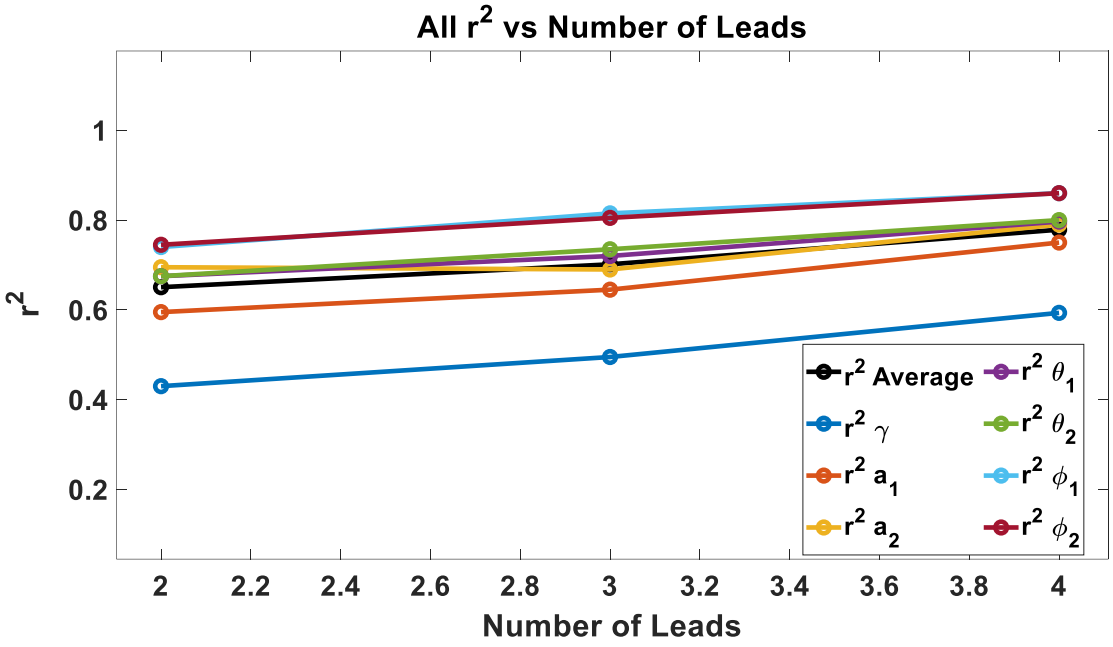

Figure 32 – Average r^2 for all IZ parameters vs number of leads used to train the 1D CNN-LSTM. Increasing the number of leads increases all the r^2 values. Values are found by averaging r^2 values in Table 5 of case numbers with the same amount of number of leads.

Overall, the r^2 of all ischemic zone parameters increased as the number of leads used in training increased. r_1^2 (γ) was the lowest in all circumstances which was noted in previous research (Chapter III). When predicting future states of ischemia, the performance of the 1D CNN-LSTM model increased as the number of leads increased. Noting the r^2 $Average$ as the overall performance of the neural network, the theoretical maximum r^2 $Average$ was found by assuming a maximum value of a, in which $a \leq 1$, and assuming the r^2 $average$ approaches an asymptote as the number of leads increases. The maximum r^2 $average$ is found with the equation $f(x) = a + \frac{b}{x}$ where x is the number of leads used in training. Maximum r^2 $average$ is shown as a in Figure 33.

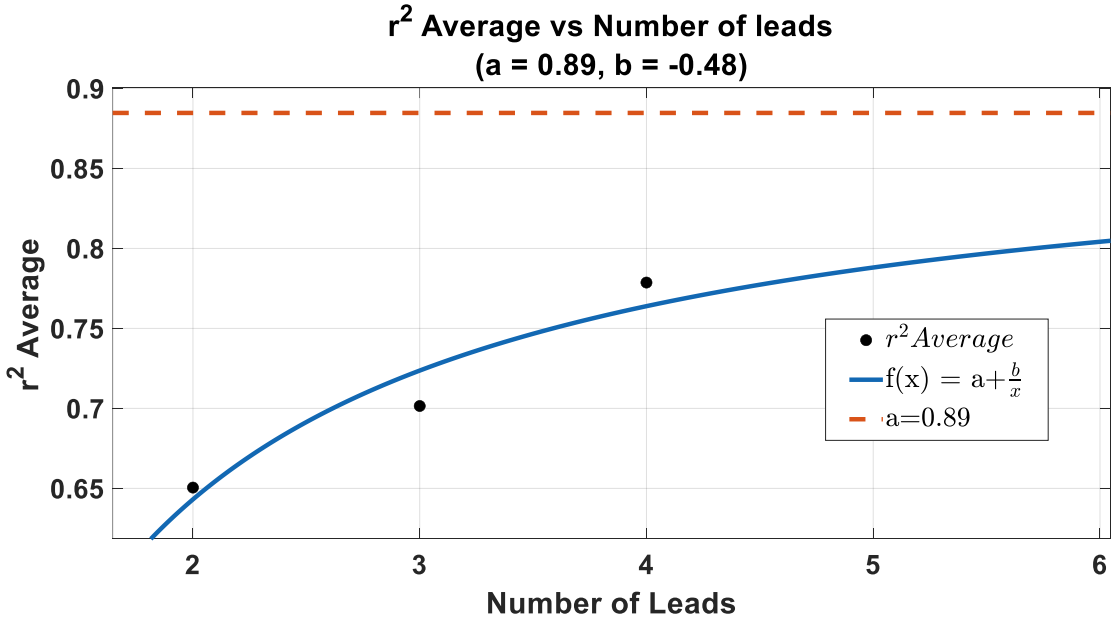

Figure 33 - r^2 *average* vs number of leads. Assuming an asymptotic maximum value a, the points were fitted using the equation $f(x) = a + \frac{b}{x}$. Theoretical maximum r^2 *average* was found to be $a = 0.89$.

Calibration of the four-lead trained model (Case 7, Table 5) was completed on the predicted values against the true values for both volume and γ in Figure 34. Volume was calculated using (66).

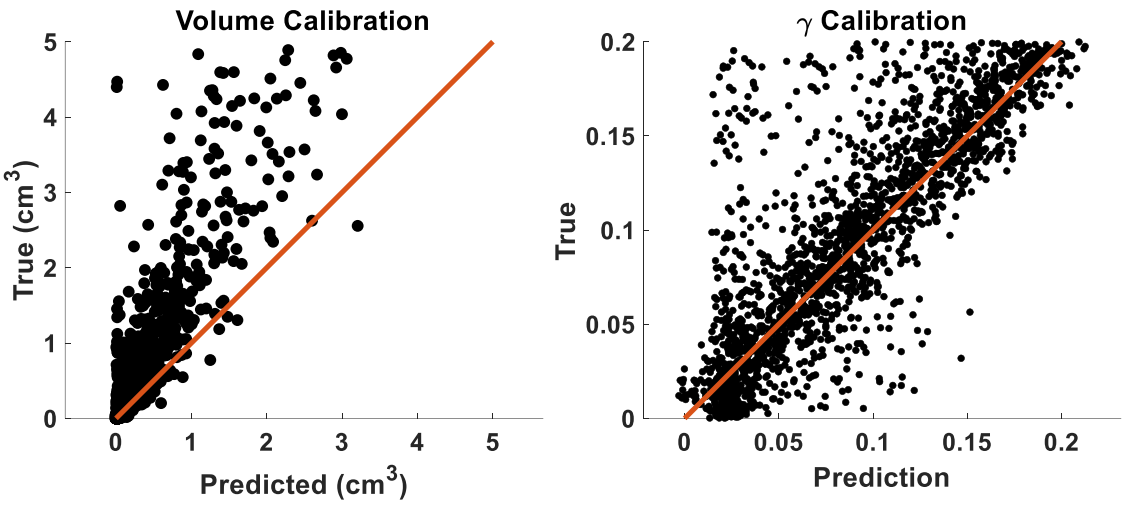

Figure 34 – Calibration of the four-lead trained model (Case 7, Table 5). The model tends to underpredict the volume. Calibration shows the prediction of the model for the variable γ performed well with some outliers.

For the four-lead trained model (Case 7, Table 5) the normalized root mean square error (NRMSE or Q) between the predicted and *in silico* (True) data are reported for each individual parameter individually as $Q_\gamma = 0.17, Q_{a_1} = 0.11, Q_{a_2} = 0.11, Q_{\theta_1} = 0.12, Q_{\theta_2} = 0.12, Q_{\phi_1} = 0.10$ and $Q_{\phi_2} = 0.10$. Overall, the models performance for predicting γ was less than the other ischemic zone parameters.

Predicting early stages of LAD occlusion

Simulating occlusion of the left descending artery (LAD) is completed through assuming quick growth from the mid-myocardial region outward[57]. Typically, LAD effects the region around the apex and interventricular region of the heart[68]. This growth may be approximated by assuming an initial point of growth and expands outwards through logistic type growth. We assumed from a starting point for the ischemic zone configuration parameters are varied using a scaling factor until the end values are obtained. For the volume parameters, an initial point of $S = 0$ of the final value is assumed and ends at $S = 1$ for the end value of the ischemic zone

volume. Likewise, the parameter γ was varied from $\gamma = .01$ to $\gamma = .15$. Figure 35 shows the logistic derived scaling value for the ischemic zone parameters.

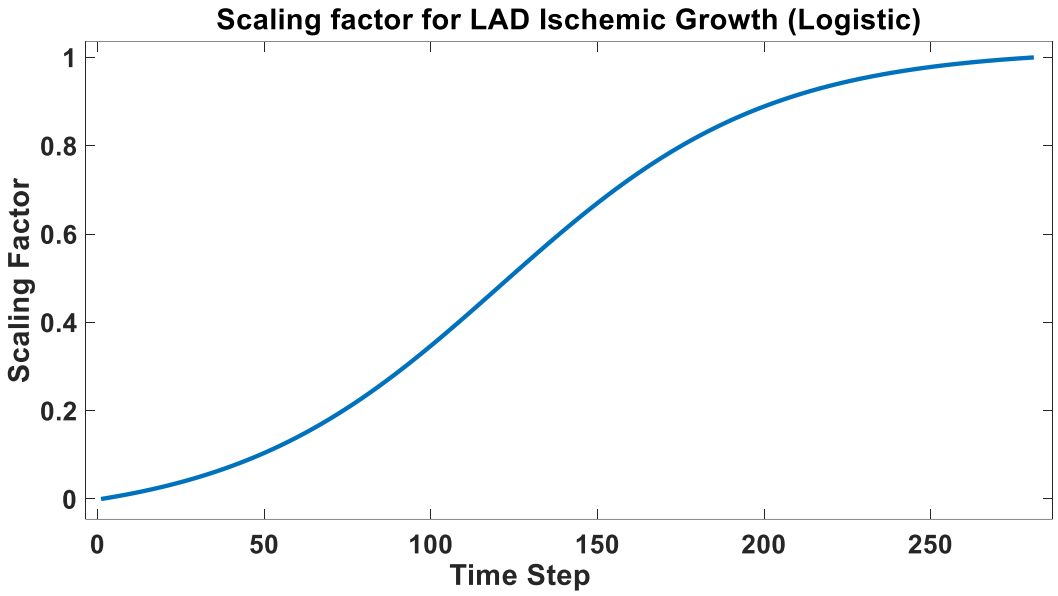

Figure 35 – Logistic scaling factor for simulating LAD IZ growth. Logistic growth is normalized for scaling γ.

Figure 36 depicts the simulated LAD growth with a beginning center point of $a_{cp} = 2.5\ cm, \theta = .6\ \pi\ rads\ and\ \phi = .5\ \pi\ rads$ and expanding out to $a_1 = 2.25\ cm, a_2 = 2.75\ cm, \theta_1 = .5\ \pi\ rads, \theta_2 = .7\ \pi\ rads, \phi_1 = .4\ \pi\ rads\ and\ \phi_2 = .6\ \pi\ rads$. The volume starts from 0 cm^3 and ends at 3.4 cm^3.

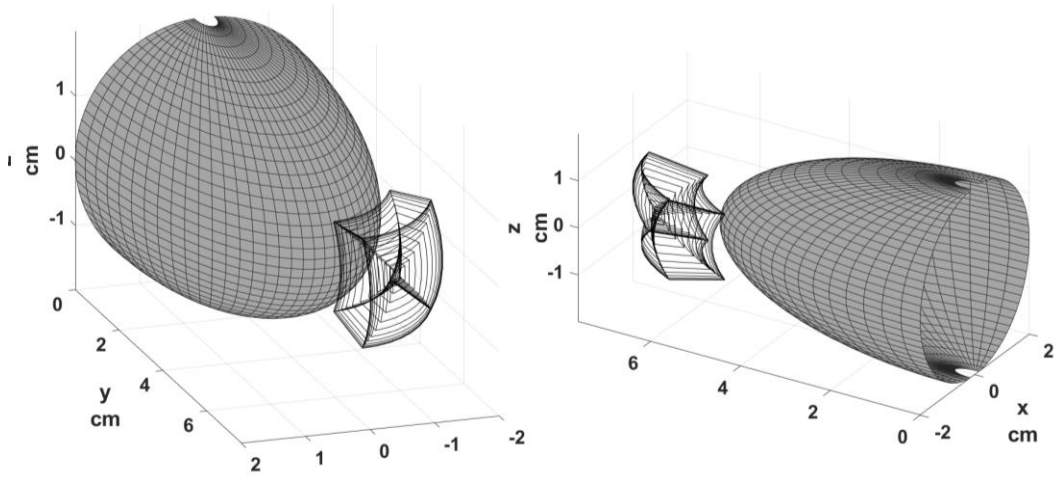

Figure 36 – Simulated LAD IZ growth.

Using the controlled ischemic growth, a database of ischemic parameters and the associated ECGs was created. The trained 1D CNN-LSTM (case 7 in Table 5) was used to predict the next time step of the LAD ischemic growth dataset. The ischemic zone parameters for the next step predictions are shown in Figure 37.

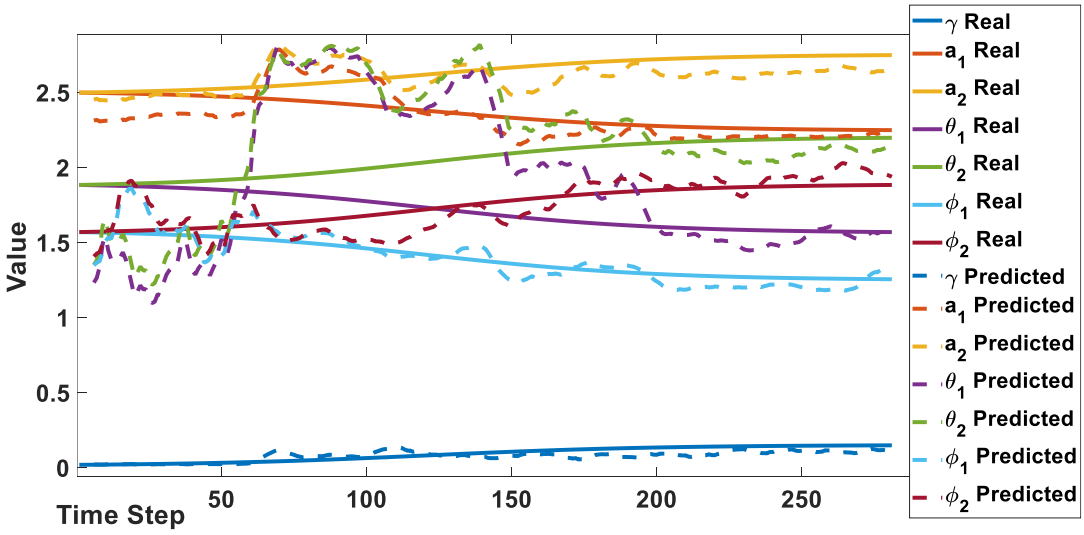

Figure 37 – 1D CNN-LSTM predictions for IZ_{t+1} parameters. Data was smoothed for clarity using a moving mean over 10 time steps.

Volume was calculated using IZ parameters $a_1, a_2, \theta_1, \theta_2, \phi_1$ and ϕ_2 and (66). Figure 38 shows the predictions of the simulated LAD growth for both volume and γ.

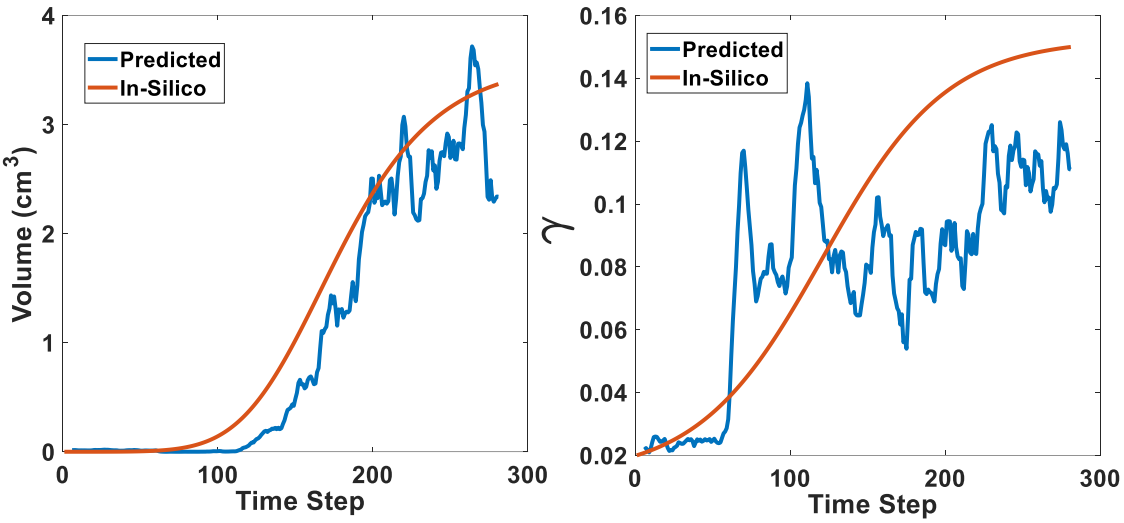

Figure 38 – Predicted and *in silico* (True) values for volume and γ of IZ_{t+1}. The r^2 for volume and γ are 0.91 and 0.40, respectively.

The mean square error (MSE) between *in silico* and predicted for both volume and γ, in Figure 38, was 0.41 and 0.0021, respectively. The NRMSE between *in silico* and predicted for both volume and γ in Figure 38 was 0.19 and 0.36, respectively. r^2 between the predicted and *in silico* curves for volume and γ in Figure 38 is 0.91 and 0.40, respectively. In the initial growth when the volume is less than 1.5 cm^3, before the first 150-time steps, the 1D CNN-LSTM model consistently underestimated the volume and overestimate γ. After the volume passes 1.5 cm^3 the 1D CNN-LSTM predicted the volume with lower error but continued to underpredicted γ. The results for volume are consistent with the calibration shown in Figure 34 as the trained model showed to underestimate the volume. γ appears to fit poorly initially but after volume passes the threshold of 1.5 cm^3 the performance predicting γ appears to become more stable but continued

to underpredict as well. In general, when the predicted volume was higher, the predicted γ shifted lower and vice versa. While undesired, the balance between over and under predicting volume and γ is understandable through normal electrocardiography theory. Smaller gradients, induced by a smaller γ, within a larger ischemic zone can produce ECG signal alternans like larger gradients within a smaller ischemic zone. Therefore, the 1D CNN-LSTM attempts to predict correctly by adjusting around the true value.

Conclusions

In conclusion, the 1D CNN-LSTM has shown to correlate previous ECG signals with future ischemic zone parameters well. The model fit training data from a directed random walk method well with the best performance using 4 leads to train a 1D CNN-LSTM with a mean $r^2\ average = 0.78$. Continuing to increase the number of leads was shown to improve the performance of the 1D CNN-LSTM to a theoretical maximum of $r^2\ average = 0.89$. The 1D CNN-LSTM model has been shown to have the ability to predict some forms of cardiac ischemia induced by LAD occlusion.

It should be noted that the current 1D CNN-LSTM can predict on ischemia away from the endocardial and epicardial boundaries, $a = 2$ and $a = 3$ respectively. Predictions near the boundary condition tend to underperform due to the size of the training data set and low occurrence of ischemic zones incorporating the boundary conditions in the training dataset. This issue could easily be addressed in future studies by incorporating more training instances that incorporate the boundaries. Performance could also be improved if the number of ischemic zone parameters was reduced but may impede further investigations into the workings of the 1D CNN-LSTM. All issues noted in previously studies still stand but were also previously addressed. All possible hindrances plan to be addressed in future studies.

CHAPTER V: CONCLUSIONS

The work presented investigated using *in silico* ECGs to theoretically determine myocardial ischemia within the left ventricle. The foundations are clearly laid out how to approach the problem of predicting the configuration, severity, and future sates of ischemia in Chapter II, Chapter III and Chapter IV. Using the materials from the introduction (Chapter I), Chapter II, Chapter III and Chapter IV show the multi-disciplinary approaches to theoretically predict myocardial ischemia using a non-invasive procedure.

In Chapter II it is demonstrated that a 2D model of the left ventricle can be used to simulate the electrical activity of the left ventricle using the BOFC reaction diffusion equations. Transmural ischemic scenarios can be impressed upon the 2D model by increasing u_o within the ischemic zone. Assuming the ischemic zone to propagate from the endocardial to epicardial region, ECG signals from a single lead were computed at various angles relative to the recording electrode. A single ratio between the T-wave amplitude and the ST segment deviation was defined. Using analytical methods, a threshold of $\frac{\partial \gamma}{\partial t} > 0.018\, min^{-1}$ was determined to be used in conjunction with typical ischemic growth to detect the early stages of transmural ischemic growth which are aligned with a single recording electrode.

Chapter III demonstrated that a simplified 3D geometry made through using skewed spherical coordinates can approximate the left ventricle. The simplified geometry is applicable to use finite difference method to solve the BOFC reaction diffusion equation. Within the boundaries of the model an ischemic zone was defined through stochastic measure to represent numerous different configurations and severity combinations. Ischemic zones induced ECG alternans that could be detected from multiple lead positions. Using 20,000 stochastically defined

ischemic zone configurations the corresponding ECGs were recorded and stored into a database. A 1D CNN was applied to predict the ischemic zone configuration from varying number of input ECG leads. It was shown that the 1D CNN stopped improving on $r^2\ average$ when increasing above two leads. The two-lead trained 1D CNN had a mean $r^2\ average = 0.85$. In addition, it was shown that most of the error in the predictions by the 1D CNN was due to low γ and/or volume under 0.02 and $2\ cm^3$, respectively.

Chapter IV focused on predicting future states of ischemia using a 1D CNN-LSTM. Through similar methods to Chapter III, ischemic zones were generated with changing isotopic volumes and severity. The volumes and severity were scaled using a directed random walk method where a scaling parameter was associated with each time step. Using the stochastic growing ischemic zones, the associated ECGs were generated for each time step which included multiple leads. A 1D CNN-LSTM was trained using five previous time steps and the associated ECG signals to predict the ischemic zone parameters for the next time step. The best performance was shown using four leads to train the 1D CNN-LSTM with an $r^2\ average = 0.78$. The 1D CNN-LSTM was used to predict *in silico* LAD growth in which volume and γ was predicted with $r^2 = 0.91$ and $r^2 = 0.40$, respectively.

WORKS CITED

(1) Virani, S. S.; Alonso, A.; Aparicio, H. J.; Benjamin, E. J.; Bittencourt, M. S.; Callaway, C. W.; Carson, A. P.; Chamberlain, A. M.; Cheng, S.; Delling, F. N.; Elkind, M. S. V.; Evenson, K. R.; Ferguson, J. F.; Gupta, D. K.; Khan, S. S.; Kissela, B. M.; Knutson, K. L.; Lee, C. D.; Lewis, T. T.; Liu, J.; Loop, M. S.; Lutsey, P. L.; Ma, J.; Mackey, J.; Martin, S. S.; Matchar, D. B.; Mussolino, M. E.; Navaneethan, S. D.; Perak, A. M.; Roth, G. A.; Samad, Z.; Satou, G. M.; Schroeder, E. B.; Shah, S. H.; Shay, C. M.; Stokes, A.; VanWagner, L. B.; Wang, N.-Y.; Tsao, C. W.; Subcommittee, O. behalf of the A. H. A. C. on E. and P. S. C. and S. S. Heart Disease and Stroke Statistics—2021 Update. *Circulation* **2021**, E254–E743. https://doi.org/10.1161/CIR.0000000000000950.

(2) Herring, N.; Paterson, D. J. ECG Diagnosis of Acute Ischaemia and Infarction: Past, Present and Future. *QJM: An International Journal of Medicine* **2006**, *99* (4), 219–230. https://doi.org/10.1093/QJMED/HCL025.

(3) Ellis, K. M. EKG Plain and Simple. 489.

(4) Buechel, E. V.; Kaiser, T.; Jackson, C.; Schmitz, A.; Kellenberger, C. J. Normal Right- and Left Ventricular Volumes and Myocardial Mass in Children Measured by Steady State Free Precession Cardiovascular Magnetic Resonance. *Journal of Cardiovascular Magnetic Resonance* **2009**, *11* (1), 19. https://doi.org/10.1186/1532-429X-11-19.

(5) Ideker, R. E.; Kong, W.; Pogwizd, S. Purkinje Fibers and Arrhythmias. *Pacing and clinical electrophysiology : PACE* **2009**, *32* (3), 283. https://doi.org/10.1111/J.1540-8159.2008.02232.X.

(6) Andersn, H. R.; Falk, E.; Nielsen, D. Right Ventricular Infarction: Frequency, Size and Topography in Coronary Heart Disease: A Prospective Study Comprising 107

Consecutive Autopsies from a Coronary Care Unit. *Journal of the American College of Cardiology* **1987**, *10* (6), 1223–1232. https://doi.org/10.1016/S0735-1097(87)80122-5.

(7) Jeffers, J. L.; Boyd, K. L.; Parks, L. J. *Right Ventricular Myocardial Infarction*; StatPearls Publishing, 2021.

(8) Greenbaum, R. A.; Ho, S. Y.; Gibson, D. G.; Becker, A. E.; Anderson, R. H. Left Ventricular Fibre Architecture in Man. *British Heart Journal* **1981**, *45* (3), 248–263. https://doi.org/10.1136/hrt.45.3.248.

(9) FitzHugh, R. Impulses and Physiological States in Theoretical Models of Nerve Membrane. *Biophysical Journal* **1961**, *1* (6), 445–466. https://doi.org/10.1016/S0006-3495(61)86902-6.

(10) FitzHugh, R. Mathematical Models of Threshold Phenomena in the Nerve Membrane. *The bulletin of mathematical biophysics 1955 17:4* **1955**, *17* (4), 257–278. https://doi.org/10.1007/BF02477753.

(11) Nagumo, J.; Arimoto, S.; Yoshizawa, S. An Active Pulse Transmission Line Simulating Nerve Axon*. *Proceedings of the IRE* **1962**, *50* (10), 2061–2070. https://doi.org/10.1109/JRPROC.1962.288235.

(12) Hodgkin, A. L.; Huxley, A. F. A Quantitative Description of Membrane Current and Its Application to Conduction and Excitation in Nerve. *The Journal of Physiology* **1952**, *117* (4), 500–544. https://doi.org/10.1113/jphysiol.1952.sp004764.

(13) Wei; Phung, D.; Tran, T.; Gupta, S.; Rana, S.; Karmakar, C.; Shilton, A.; Yearwood, J.; Dimitrova, N.; Ho, T. B.; Venkatesh, S.; Berk, M. Guidelines for Developing and Reporting Machine Learning Predictive Models in Biomedical Research: A Multidisciplinary View. *J Med Internet Res 2016;18(12):e323*

https://www.jmir.org/2016/12/e323 **2016**, *18* (12), e5870. https://doi.org/10.2196/JMIR.5870.

(14) Understanding LSTM and its diagrams | by Shi Yan | ML Review https://blog.mlreview.com/understanding-lstm-and-its-diagrams-37e2f46f1714 (accessed 2021 -08 -31).

(15) Loeffler, S.; Starobin, J. Evaluation of Severity of Cardiac Ischemia Using In Silico ECG Computed from 2D Reaction Diffusion Model. In *2020 Computing in Cardiology Conference (CinC)*; Computing in Cardiology, 2020; Vol. 47. https://doi.org/10.22489/cinc.2020.033.

(16) Cardiovascular diseases (CVDs) https://www.who.int/news-room/fact-sheets/detail/cardiovascular-diseases-(cvds) (accessed 2020 -04 -06).

(17) Plonsey, R.; Barr, R. C. *Bioelectricity: A Quantitative Approach*; Springer US, 2007. https://doi.org/10.1007/978-0-387-48865-3.

(18) Garny, A.; Noble, D.; Kohl, P. Dimensionality in Cardiac Modelling. *Progress in Biophysics and Molecular Biology*. Elsevier Ltd January 1, 2005, pp 47–66. https://doi.org/10.1016/j.pbiomolbio.2004.06.006.

(19) Zeile, C.; Scholz, E.; Sager, S. A Simplified 2D Heart Model of the Wolff-Parkinson-White Syndrome. *IFAC-PapersOnLine* **2016**, *49* (26), 26–31. https://doi.org/10.1016/j.ifacol.2016.12.098.

(20) Klabunde, R. E. Cardiac Electrophysiology: Normal and Ischemic Ionic Currents and the ECG. *Advances in Physiology Education* **2017**, *41* (1), 29–37. https://doi.org/10.1152/advan.00105.2016.

(21) Shaw, R. M.; Rudy, Y. Electrophysiologic Effects of Acute Myocardial Ischemia: A Theoretical Study of Altered Cell Excitability and Action Potential Duration. *Cardiovascular Research* **1997**, *35* (2), 256–272. https://doi.org/10.1016/S0008-6363(97)00093-X.

(22) Bueno-Orovio, A.; Cherry, E. M.; Fenton, F. H. Minimal Model for Human Ventricular Action Potentials in Tissue. *Journal of Theoretical Biology* **2008**, *253* (3), 544–560. https://doi.org/10.1016/j.jtbi.2008.03.029.

(23) Reimer, K. A.; Lowe, J. E.; Rasmussen, M. M.; Jennings, R. B. The Wavefront Phenomenon of Ischemic Cell Death. 1. Myocardial Infarct Size vs Duration of Coronary Occlusion in Dogs. *Circulation* **1977**, *56* (5), 786–794. https://doi.org/10.1161/01.CIR.56.5.786.

(24) Loeffler, S.; Starobin, J. Reaction-Diffusion Informed Approach to Determine Myocardial Ischemia Using Stochastic in silico ECGs and CNNs. *Computers in Biology and Medicine* **2021**, *136*, 104635. https://doi.org/10.1016/J.COMPBIOMED.2021.104635.

(25) Benjamin, E. J.; Muntner, P.; Alonso, A.; Bittencourt, M. S.; Callaway, C. W.; Carson, A. P.; Chamberlain, A. M.; Chang, A. R.; Cheng, S.; Das, S. R.; Delling, F. N.; Djousse, L.; Elkind, M. S. V.; Ferguson, J. F.; Fornage, M.; Jordan, L. C.; Khan, S. S.; Kissela, B. M.; Knutson, K. L.; Kwan, T. W.; Lackland, D. T.; Lewis, T. T.; Lichtman, J. H.; Longenecker, C. T.; Loop, M. S.; Lutsey, P. L.; Martin, S. S.; Matsushita, K.; Moran, A. E.; Mussolino, M. E.; O'Flaherty, M.; Pandey, A.; Perak, A. M.; Rosamond, W. D.; Roth, G. A.; Sampson, U. K. A.; Satou, G. M.; Schroeder, E. B.; Shah, S. H.; Spartano, N. L.; Stokes, A.; Tirschwell, D. L.; Tsao, C. W.; Turakhia, M. P.; VanWagner, L. B.; Wilkins, J. T.; Wong, S. S.; Virani, S. S. Heart Disease and Stroke Statistics-2019 Update: A

Report From the American Heart Association. *Circulation* **2019**. https://doi.org/10.1161/CIR.0000000000000659.

(26) Khan, M. A.; Hashim, M. J.; Mustafa, H.; Baniyas, M. Y.; Al Suwaidi, S. K. B. M.; AlKatheeri, R.; Alblooshi, F. M. K.; Almatrooshi, M. E. A. H.; Alzaabi, M. E. H.; Al Darmaki, R. S.; Lootah, S. N. A. H. Global Epidemiology of Ischemic Heart Disease: Results from the Global Burden of Disease Study. *Cureus* **2020**, *12* (7). https://doi.org/10.7759/cureus.9349.

(27) Boersma, E.; Maas, A. C. P.; Deckers, J. W.; Simoons, M. L. Early Thrombolytic Treatment in Acute Myocardial Infarction: Reappraisal of the Golden Hour. *Lancet* **1996**, *348* (9030), 771–775. https://doi.org/10.1016/S0140-6736(96)02514-7.

(28) Selvester, R. H.; Wagner, G. S.; Hindman, N. B. The Selvester QRS Scoring System for Estimating Myocardial Infarct Size: The Development and Application of the System. *Archives of Internal Medicine* **1985**, *145* (10), 1877–1881. https://doi.org/10.1001/archinte.1985.00360100147024.

(29) Xia, X.; Wieslander, B.; Strauss, D. G.; Wagner, G. S.; Zareba, W.; Moss, A. J.; Couderc, J. P. Automatic QRS Selvester Scoring System in Patients with Left Bundle Branch Block. *Europace* **2016**, *18* (2), 308–314. https://doi.org/10.1093/europace/euv040.

(30) Kara, V.; Ni, H.; Alday, E. A. P.; Zhang, H. ECG Imaging to Detect the Site of Ventricular Ischemia Using Torso Electrodes: A Computational Study. *Frontiers in Physiology* **2019**, *10* (FEB), 50. https://doi.org/10.3389/fphys.2019.00050.

(31) Malmivuo, J.; Plonsey, R. *Bioelectromagnetism: Principles and Applications of Bioelectric and Biomagnetic Fields*; 2012. https://doi.org/10.1093/acprof:oso/9780195058239.001.0001.

(32) Clayton, R. H.; Holden, A. V. Computational Framework for Simulating the Mechanisms and ECG of Re-Entrant Ventricular Fibrillation. *Physiological Measurement* **2002**, *23* (4), 707–726. https://doi.org/10.1088/0967-3334/23/4/310.

(33) Pullan, A. J.; Cheng, L. K.; Nash, M. P.; Ghodrati, A.; MacLeod, R.; Brooks, D. H. The Inverse Problem of Electrocardiography. In *Comprehensive Electrocardiology*; Springer London, 2010; pp 299–344. https://doi.org/10.1007/978-1-84882-046-3_9.

(34) Moody, G. B.; Mark, R. G. The Impact of the MIT-BIH Arrhythmia Database. *IEEE Engineering in Medicine and Biology Magazine*. 2001, pp 45–50. https://doi.org/10.1109/51.932724.

(35) Luo, C.; Jiang, H.; Li, Q.; Rao, N. Multi-Label Classification of Abnormalities in 12-Lead ECG Using 1D CNN and LSTM. In *Lecture Notes in Computer Science (including subseries Lecture Notes in Artificial Intelligence and Lecture Notes in Bioinformatics)*; Springer, 2019; Vol. 11794 LNCS, pp 55–63. https://doi.org/10.1007/978-3-030-33327-0_7.

(36) Mincholé, A.; Camps, J.; Lyon, A.; Rodríguez, B. Machine Learning in the Electrocardiogram. *Journal of Electrocardiology*. Churchill Livingstone Inc. November 1, 2019, pp S61–S64. https://doi.org/10.1016/j.jelectrocard.2019.08.008.

(37) Kiranyaz, S.; Ince, T.; Gabbouj, M. Real-Time Patient-Specific ECG Classification by 1-D Convolutional Neural Networks. *IEEE Transactions on Biomedical Engineering* **2016**, *63* (3), 664–675. https://doi.org/10.1109/TBME.2015.2468589.

(38) Xia, Y.; Zhang, H.; Xu, L.; Gao, Z.; Zhang, H.; Liu, H.; Li, S. An Automatic Cardiac Arrhythmia Classification System with Wearable Electrocardiogram. *IEEE Access* **2018**, *6*, 16529–16538. https://doi.org/10.1109/ACCESS.2018.2807700.

(39) Jafarian, K.; Vahdat, V.; Salehi, S.; Mobin, M. Automating Detection and Localization of Myocardial Infarction Using Shallow and End-to-End Deep Neural Networks. *Applied Soft Computing Journal* **2020**, *93*, 106383. https://doi.org/10.1016/j.asoc.2020.106383.

(40) Lorente, M.; Escalona, C.; Zabalza-Cerdeiriña, M.; Álvarez-Moro, J. Left Ventricle Morphometry in Healthy Humans. Long Axis, Contrast Enhanced CT Study. *Scientific Medical Data* **2017**. https://doi.org/10.24175/sbd.2017.000004.

(41) Støylen, A.; Mølmen, H. E.; Dalen, H. Importance of Length and External Diameter in Left Ventricular Geometry. Normal Values from the HUNT Study. *Open Heart* **2016**, *3* (2), 465. https://doi.org/10.1136/openhrt-2016-000465.

(42) Kou, S.; Caballero, L.; Dulgheru, R.; Voilliot, D.; De Sousa, C.; Kacharava, G.; Athanassopoulos, G. D.; Barone, D.; Baroni, M.; Cardim, N.; Gomez De Diego, J. J.; Hagendorff, A.; Henri, C.; Hristova, K.; Lopez, T.; Magne, J.; De La Morena, G.; Popescu, B. A.; Penicka, M.; Ozyigit, T.; Rodrigo Carbonero, J. D.; Salustri, A.; Van De Veire, N.; Von Bardeleben, R. S.; Vinereanu, D.; Voigt, J.-U.; Zamorano, J. L.; Donal, E.; Lang, R. M.; Badano, L. P.; Lancellotti, P. Echocardiographic Reference Ranges for Normal Cardiac Chamber Size: Results from the NORRE Study. *European Heart Journal - Cardiovascular Imaging* **2014**, *15* (6), 680–690. https://doi.org/10.1093/ehjci/jet284.

(43) Bohm, P.; Schneider, G.; Linneweber, L.; Rentzsch, A.; Krämer, N.; Abdul-Khaliq, H.; Kindermann, W.; Meyer, T.; Scharhag, J. Right and Left Ventricular Function and Mass in Male Elite Master Athletes: A Controlled Contrast-Enhanced Cardiovascular Magnetic Resonance Study. *Circulation* **2016**, *133* (20), 1927–1935. https://doi.org/10.1161/CIRCULATIONAHA.115.020975.

(44) Kawel-Boehm, N.; Maceira, A.; Valsangiacomo-Buechel, E. R.; Vogel-Claussen, J.; Turkbey, E. B.; Williams, R.; Plein, S.; Tee, M.; Eng, J.; Bluemke, D. A. Normal Values for Cardiovascular Magnetic Resonance in Adults and Children. *Journal of Cardiovascular Magnetic Resonance*. BioMed Central Ltd. April 18, 2015, p 29. https://doi.org/10.1186/s12968-015-0111-7.

(45) Gheorghe, A. G.; Fuchs, A.; Jacobsen, C.; Kofoed, K. F.; Møgelvang, R.; Lynnerup, N.; Banner, J. Cardiac Left Ventricular Myocardial Tissue Density, Evaluated by Computed Tomography and Autopsy. *BMC Medical Imaging* **2019**, *19* (1). https://doi.org/10.1186/s12880-019-0326-4.

(46) Andersn, H. R.; Falk, E.; Nielsen, D. Right Ventricular Infarction: Frequency, Size and Topography in Coronary Heart Disease: A Prospective Study Comprising 107 Consecutive Autopsies from a Coronary Care Unit. *Journal of the American College of Cardiology* **1987**, *10* (6), 1223–1232. https://doi.org/10.1016/S0735-1097(87)80122-5.

(47) Sedmera, D.; Gourdie, R. G. Why Do We Have Purkinje Fibers Deep in Our Heart? *Physiological Research*. 2014. https://doi.org/10.33549/physiolres.932686.

(48) Janse, M. J.; Coronel, R.; Opthof, T.; Sosunov, E. A.; Anyukhovsky, E. P.; Rosen, M. R. Repolarization Gradients in the Intact Heart: Transmural or Apico-Basal? *Progress in Biophysics and Molecular Biology*. Prog Biophys Mol Biol May 2012, pp 6–15. https://doi.org/10.1016/j.pbiomolbio.2012.03.001.

(49) Boukens, B. J.; Sulkin, M. S.; Gloschat, C. R.; Ng, F. S.; Vigmond, E. J.; Efimov, I. R. Transmural APD Gradient Synchronizes Repolarization in the Human Left Ventricular Wall. *Cardiovascular Research* **2015**, *108* (1), 188–196. https://doi.org/10.1093/cvr/cvv202.

(50) Van Rossum, G.; Drake Jr, F. L. *Python Tutorial*; Centrum voor Wiskunde en Informatica Amsterdam, The Netherlands, 1995.

(51) Chollet, F.; others. Keras. 2015.

(52) Perez Alday, E. A.; Whittaker, D. G.; Benson, A. P.; Colman, M. A. Effects of Heart Rate and Ventricular Wall Thickness on Non-Invasive Mapping: An in Silico Study. *Frontiers in Physiology* **2019**, *10* (APR), 308. https://doi.org/10.3389/fphys.2019.00308.

(53) Nagata, Y. The Influence of the Inhomogeneities of Electrical Conductivity Within the Torso on the Electrocardiogram as Evaluated from the View Point of the Transfer Impedance Vector. *Japanese Heart Journal* **1970**, *11* (5), 489–505. https://doi.org/10.1536/ihj.11.489.

(54) Carmeliet, E. Cardiac Ionic Currents and Acute Ischemia: From Channels to Arrhythmias. *Physiological Reviews*. American Physiological Society 1999, pp 917–1017. https://doi.org/10.1152/physrev.1999.79.3.917.

(55) Carmeliet, E. Cardiac Ionic Currents and Acute Ischemia: From Channels to Arrhythmias. *Physiological Reviews* **1999**, *79* (3), 917–1017. https://doi.org/10.1152/physrev.1999.79.3.917.

(56) Yeap, X.-Y.; Dehn, S.; Adelman, J.; Lipsitz, J.; Thorp, E. B. Quantitation of Acute Necrosis After Experimental Myocardial Infarction; 2013; pp 115–133. https://doi.org/10.1007/978-1-62703-383-1_9.

(57) Aras, K.; Burton, B.; Swenson, D.; MacLeod, R. Spatial Organization of Acute Myocardial Ischemia. *Journal of electrocardiology* **2016**, *49* (3), 323. https://doi.org/10.1016/J.JELECTROCARD.2016.02.014.

(58) Burton, B. M.; Aras, K. K.; Good, W. W.; Tate, J. D.; Zenger, B.; Macleod, R. S. A Framework for Image-Based Modeling of Acute Myocardial Ischemia Using Intramurally Recorded Extracellular Potentials. **2048**. https://doi.org/10.1007/s10439-018-2048-0.

(59) Burton, B. M. SUBJECT-SPECIFIC MODELING OF PARTIAL THICKNESS CARDIAC ISCHEMIA: FROM EXPERIMENT TO BODY SURFACE. **2018**.

(60) Rodríguez, B.; Trayanova, N.; Noble, D. Modeling Cardiac Ischemia. **2006**. https://doi.org/10.1196/annals.1380.029.

(61) Niederer, S. Regulation of Ion Gradients across Myocardial Ischemic Border Zones: A Biophysical Modelling Analysis. *PLOS ONE* **2013**, *8* (4), e60323. https://doi.org/10.1371/JOURNAL.PONE.0060323.

(62) Malmivuo, J.; Plonsey, R. *Bioelectromagnetism: Principles and Applications of Bioelectric and Biomagnetic Fields*; 2012. https://doi.org/10.1093/acprof:oso/9780195058239.001.0001.

(63) Plonsey, R.; Barr, R. C. *Bioelectricity: A Quantitative Approach*; 2007. https://doi.org/10.1007/978-0-387-48865-3.

(64) Li, D.; Zhang, J.; Zhang, Q.; Wei, X. Classification of ECG Signals Based on 1D Convolution Neural Network. In *2017 IEEE 19th International Conference on e-Health Networking, Applications and Services, Healthcom 2017*; Institute of Electrical and Electronics Engineers Inc., 2017; Vol. 2017-December, pp 1–6. https://doi.org/10.1109/HealthCom.2017.8210784.

(65) Kiranyaz, S.; Ince, T.; Gabbouj, M. Real-Time Patient-Specific ECG Classification by 1-D Convolutional Neural Networks. *IEEE Transactions on Biomedical Engineering* **2016**, *63* (3), 664–675. https://doi.org/10.1109/TBME.2015.2468589.

(66) Hochreiter, S.; Schmidhuber, J. Long Short-Term Memory. *Neural Computation* **1997**, *9* (8), 1735–1780. https://doi.org/10.1162/NECO.1997.9.8.1735.

(67) Huang, S.-Y.; Zou, X.-W.; Jin, Z.-Z. Directed Random Walks in Continuous Space. *Physical Review E* **2002**, *65* (5), 052105. https://doi.org/10.1103/PhysRevE.65.052105.

(68) Villa, A. D.; Sammut, E.; Nair, A.; Rajani, R.; Bonamini, R.; Chiribiri, A. Coronary Artery Anomalies Overview: The Normal and the Abnormal. **2016**. https://doi.org/10.4329/wjr.v8.i6.537.

APPENDIX A: ADDITIONAL INFORMATION FOR CHAPTER III: REACTION-DIFFUSION INFORMED APPROACH TO DETERMINE MYOCARDIAL ISCHEMIA USING STOCHASTIC *IN SILICO* ECGS AND CNNS[24]

Metric Tensor

Metric tensor is presented in matrix form with "i" and "j" vary by a, θ, φ, respectively.

$$g_{ij} = \begin{matrix} Cos[\phi]^2 + (Cos[\theta]^2 + s^2 Sin[\theta]^2) Sin[\phi]^2 & a(s^2-1)Cos[\theta]Sin[\theta]Sin[\phi]^2 & a(s^2-1)Cos[\phi]Sin[\theta]^2 Sin[\phi] \\ a(s^2-1)Cos[\theta]Sin[\theta]Sin[\phi]^2 & a^2(s^2 Cos[\theta]^2 + Sin[\theta]^2)Sin[\phi]^2 & a^2(s^2-1)Cos[\theta]Cos[\phi]Sin[\theta]Sin[\phi] \\ a(s^2-1)Cos[\phi]Sin[\theta]^2 Sin[\phi] & a^2(s^2-1)Cos[\theta]Cos[\phi]Sin[\theta]Sin[\phi] & a^2(Cos[\phi]^2(Cos[\theta]^2 + s^2 Sin[\theta]^2) + Sin[\phi]^2) \end{matrix}$$

Inverse Metric Tensor

Inverse metric tensor is presented in matrix form with "i" and "j" vary by a, θ, φ, respectively.

$$g^{ij} = \begin{matrix} Cos[\phi]^2 + \frac{(s^2 Cos[\theta]^2 + Sin[\theta]^2)Sin[\phi]^2}{s^2} & -\frac{(-1+s^2)Cos[\theta]Sin[\theta]}{as^2} & -\frac{(-1+s^2)Cos[\phi]Sin[\theta]^2 Sin[\phi]}{as^2} \\ -\frac{(-1+s^2)Cos[\theta]Sin[\theta]}{as^2} & \frac{Csc[\phi]^2(Cos[\theta]^2 + s^2 Sin[\theta]^2)}{a^2 s^2} & -\frac{(-1+s^2)Cos[\theta]Cot[\phi]Sin[\theta]}{a^2 s^2} \\ -\frac{(-1+s^2)Cos[\phi]Sin[\theta]^2 Sin[\phi]}{as^2} & -\frac{(-1+s^2)Cos[\theta]Cot[\phi]Sin[\theta]}{a^2 s^2} & \frac{Cos[\phi]^2(s^2 Cos[\theta]^2 + Sin[\theta]^2) + s^2 Sin[\phi]^2}{a^2 s^2} \end{matrix}$$

Christoffel Symbol

The Christoffel symbols are presented in a matrix form for each upper index. "i" and "j" vary by a, θ, φ, respectively.

$$\Gamma^{a}_{ij} = \begin{pmatrix} 0 & 0 & 0 \\ 0 & -a & 0 \\ 0 & 0 & -a\,Sin[\theta]^2 \end{pmatrix} \qquad \Gamma^{\theta}_{ij} = \begin{pmatrix} 0 & 0 & a^{-1} \\ 0 & 0 & Cot[\varphi] \\ a^{-1} & Cot[\varphi] & 0 \end{pmatrix}$$

$$\Gamma^{\varphi}_{ij} = \begin{pmatrix} 0 & a^{-1} & 0 \\ a^{-1} & 0 & 0 \\ 0 & 0 & \frac{-Sin[2\theta]}{2} \end{pmatrix}$$

Discretized Laplacian for skewed spherical coordinates

$$\widehat{\nabla}^2 u_{ijk}^t = g^{aa}{}_{ijk}\frac{u_{i+1jk}^t - 2\,u_{ijk}^t + u_{i-1jk}^t}{\Delta a^2} + g^{\theta\theta}{}_{ijk}\frac{u_{ij+1k}^t - 2\,u_{ijk}^t + u_{ij-1k}^t}{\Delta\theta^2}$$

$$+ g^{\phi\phi}{}_{ijk}\frac{u_{ijk+1}^t - 2\,u_{ijk}^t + u_{ijk-1}^t}{\Delta\phi^2}$$

$$+ 2g^{a\theta}{}_{ijk}\frac{u_{i+1j+1k}^t - u_{i+1j-1k}^t - u_{i-1j+1k}^t + u_{i-1j-1k}^t}{4\Delta a\Delta\theta}$$

$$+ 2g^{a\phi}{}_{ijk}\frac{u_{i+1jk+1}^t - u_{i+1jk-1}^t - u_{i-1jk+1}^t + u_{i-1jk-1}^t}{4\Delta a\Delta\phi}$$

$$+ 2g^{\theta\phi}{}_{ijk}\frac{u_{ij+1k+1}^t - u_{ij+1k-1}^t - u_{ij-1k+1}^t + u_{ij-1k-1}^t}{4\Delta\theta\Delta\phi}$$

$$+ \left(g^{\theta\theta}{}_{ijk}\,a_{ijk} + g^{\phi\phi}{}_{ijk}a_{ijk}\,Sin\left[\phi_{ijk}\right]^2\right)\frac{u_{i+1jk}^t - u_{i-1jk}^t}{2\Delta a}$$

$$- 2\left(\frac{g^{a\phi}{}_{ijk}}{a_{ijk}} + g^{\theta\phi}{}_{ijk}Cot\left[\phi_{ijk}\right]\right)\frac{u_{ij+1k}^t - u_{ij-1k}^t}{2\Delta\theta}$$

$$+ \left(\frac{g^{\phi\phi}{}_{ijk}Sin\left[2\phi_{ijk}\right]}{2} - \frac{2\,g^{a\theta}{}_{ijk}}{a_{ijk}}\right)\frac{u_{ijk+1}^t - u_{ijk-1}^t}{2\Delta\phi}$$

Other BOFC Equations

$$\tau_v^- = (1 - H[u - \theta_v^-])\tau_{v_1}^- + H[u - \theta_v^-]\tau_{v_2}^-$$

$$\tau_w^- = \tau_{w_1}^- + (\tau_{w_2}^- - \tau_{w_1}^-)(1 + \tanh[k_w^-(u - u_w^-)])/2$$

$$\tau_{so} = \tau_{so_1} + (\tau_{so_2} - \tau_{so_1})(1 + \tanh[k_{so}(u - u_{so})])/2$$

$$\tau_s = (1 - H[u - \theta_w])\tau_{s_1} + H[u - \theta_w]\tau_{s_2}$$

$$\tau_o = (1 - H[u - \theta_o])\tau_{o_1} + H[u - \theta_o]\tau_{o_2}$$

$$v_\infty = 1 - H[u - \theta_v^-]$$

$$w_\infty = (1 - H[u - \theta_o])\left(1 - \frac{u}{\tau_{w\infty}}\right) + H[u - \theta_o]w_\infty^*$$